DC Dielectrophoretic Assisted

Anti-Fouling Filtration System

A Thesis

Presented to the Faculty of

California Polytechnic State University

San Luis Obispo

In Partial Fulfillment of the Requirements for the Degree

Master of Science in Engineering, with Specialization in Biomedical Engineering

by

Nathan M. Cohen

March 2012

COMMITTEE MEMBERSHIP

TITLE:	**DC Dielectrophoretic assisted Anti-Fouling filtration system**
AUTHOR:	**Nathan M. Cohen**
DATE SUBMITTED:	**March 2012**
COMMITTEE CHAIR:	**David Clague, Ph.D.** **Associate Professor, Biomedical and General Engineering** **California Polytechnic State University, San Luis Obispo**
COMMITTEE MEMBER:	**Lanny Griffin, Ph.D.** **Professor & Chair, Biomedical and General Engineering** **California Polytechnic State University, San Luis Obispo**
COMMITTEE MEMBER:	**Lily Laiho, Ph.D.** **Associate Professor, Biomedical and General Engineering** **California Polytechnic State University, San Luis Obispo**

ABSTRACT

DC DIELECTROPHORETIC ASSISTED ANTI-FOULING FILTRATION SYSTEM

Nathan M. Cohen

Filtration processes, whether on the microfluidic, clinical treatment systems, or industrial scale (e.g., point-of-care diagnostics, dialysis, and biopharmaceutical manufacturing, respectively), are often inseparable from membrane clogging (fouling). As a consequence, most, if not all, filtration systems require frequent maintenance to maintain functionality and efficiency. The thesis of this project hypothesizes that Dielectrophoresis can be combined with standard filtration to reduce filter fouling, extending membrane life, and enabling continuous operation. This project investigates a method to reduce fouling, add specificity and efficiency, and decrease the cost and challenge of filtration based biofluid separations.

To substantiate this thesis, we designed, fabricated, and tested a filtration system to filter micron diameter particles in suspension using Millipore™ membranes together with fabricated electrodes in a cross-flow filtration system. This prototype device elicits a repulsive dielectrophoretic (DEP) force via the application of a direct current (5-20 volts) sourced from a computer controlled voltage sequencer, designed to levitate and remove larger particles ($> 6\ \mu$m) before particulate-membrane interaction. Analysis of the results shows a sufficient decrease in particles adhered to the filtration membrane, as compared to control, suggesting DC DEP may be a valid effector in this device. We are convinced that further research will augment the results validating the proof-of-concept thesis presented herein.

ACKNOWLEDGEMENTS

I would like to thank Dr. David Clague for his guidance and support throughout this project. Without his energy and creativity, the ideas that sparked and sustained the project would not have existed.

I would also like to thank my other committee members, Dr. Lanny Griffin and Dr. Lily Laiho, who have donated their time and resources toward this project.

I would like to thank my friends and family who have always supported me through my career without ever a doubt or reservation.

Finally, I would like to thank Kris Patel and Robby Nielsen for their assistance with software modeling and CNC fabrication, respectively.

TABLE OF CONTENTS

LIST OF TABLES

TABLE OF FIGURES

1 Introduction

1.1 Hypothesis

Direct Current Dielectrophoresis (DC DEP) can be combined with continuous flow micro-filtration to eliminate micro-filtration fouling while performing filtration of micron scale from sub-micron particulates.

1.2 Goals

1. Design and fabricate a cross-flow microfiltration system.

2. Design and integrate electrodes to create a DC DEP force field to actively repel larger (micron scale) particulates from the surface of the membrane filter to mitigate fouling (clogging).

3a. Fabricate the system using the manufacturing tools available at Cal Poly.

3b. Validate functionality of unassisted microfiltration system.

4. Integrate electrodes and perform initial concept validating experiments using the necessary relevant imaging, detection, and diagnostic tools.

1.3 Motivation

This project was inspired from an industry derived need for a device that could separate blood cells from plasma in a continuous fashion, while simultaneously scanning for cancerous cells. Ultimately, it was desired to recombine the cell fraction with the blood plasma and return the cleansed blood back to the patient. The apparatus would be required to not harm the blood cells, protect against contamination, and have highly sensitive detection capabilities. The concept is highly sophisticated, but its foundation greatly depends on the ability to effectively separate specific cells from a complex fluid, blood.

1.4 Overview

This work focuses on the separation challenges associated with separating micron scale, i.e., cells, from sub-micron scale, e.g., protein, in a continuous filtration system while preventing micro-filtration fouling. We are focused on exploiting the relatively short-range forces (e.g., 40 to 50 μm effective range) of Dielectrophoresis (DEP) to create a non-fouling microfiltration system that addresses membrane fouling. Significant research into the areas of DEP and filtration was performed to substantiate the motivation and design of the device. This project encompasses the entirety of the iterative design process, from the initial concept through testing and validation, and suggested future work.

Immediately following in the Background section is a discussion of membrane filtration and fouling, applications of filtration, specific examples related to this project and the Cal Poly Biofluidics group, including a discussion of biofluids possibly used in these processing and diagnostics devices (Section 2.1 through 2.5). A discussion of

Dielectrophoresis theory will follow, including a presentation of multiphysics software models used in the development of the prototype, and a detailed review of select case studies where DEP is used. Following the Background, the Materials and Methods section describes the design development, fabrication, and validation of the prototype device. Next, the Results section displays the experimental findings of the testing and validation, followed by the Discussion and Conclusion, where the successes and shortcomings of this project will be addressed and future opportunities explored.

2 Background

2.1 Filtration and Fouling

Fouling is defined as the sufficient accumulation of solutes on the surface of a filtration membrane to reduce or prevent filter function [1], e.g., fouling reduces flux, selectivity, and overall effectiveness. This buildup of particulates on filter surfaces results in the need for higher pressure pumps upstream of the filter, increase cost of maintenance, and shorter membrane lifetimes [2]. Given that nearly all industries –- from food and beverage industry (e.g. dairy products) to the pharmaceutical industry to municipal water facilities –- use filtration in key steps in their processes, fouling and strategies for fouling mitigation are of significant importance [3-5]. (Many other industries must use filtration in accessory processes and treatments.)

Physical filtration is the traditional gold standard approach to separating particulate matter of different sizes from each other. Having said that, artificial physical filtration suffers from serious limitations; namely, 1) Larger particulates in the retentate

(the fraction of the suspension that does not pass through the membrane) form a gel-like layer on the filter surface, fouling the filter and rendering it ineffective, and 2) unlike physiological filtration membranes such as collagen/proteoglycan matrices, artificial membranes do not self-repair. Consequently, physiological filtration membranes/systems, such as the Bowman's Capsule in the kidneys, are vastly superior compared to artificial membranes.

While the overall users of filtration processes encompass an incredibly large scope of industries, this thesis project focuses on reusable micro-filtration as related to the medical and health industries. Filtration of bio-fluids, such as blood, are often subject to fouling due to the large number of particulates, biological nature of the particulates, and surface interactions of the particulates with common filters. In filtration, hydrodynamic forces from applied pressure gradients force particulates against surfaces (filtration membranes and fluid routing walls) and result in an energetically favorable interactions between particulates and surfaces, resulting in particle accumulation and possible damage, e.g., cell damage. Consequently, new approaches need to be developed to enable separations in complex fluids, e.g. biofluids, while preventing cell damage and membrane fouling. Through the separation of target constituents from complex, particle-laden solutions, analysis tools can be used to perform diagnostic tests and other functions on the target, producing quantitative and qualitative results.

Analytic biofluid devices can be bench-scale down to the micro- and even nanoscale. No matter the size of devices, fouling occurs and can render the product unusable, which is why most medical devices for handling biofluids are disposable. In keeping with the capabilities of the Cal Poly Biofluidics laboratory, filtration and assisted

filtration research is performed at the centimeter to micron length scales or microfluidic device length scale. In contrast, such forces of interaction impart negligible effects on the macro-scale, e.g. centimeters to meters length scale. The device developed in this project is being fabricated on a larger scale than microfluidics, but can be applied to both smaller and larger scale systems. In the device presented here, the fluidics are largely on the macro-scale; however, the pores of the membrane are on the micron scale. This "mixed" system allows for flexibility in design and fabrication, allowing us to capitalize on the benefits of both size scales, without some of the sacrifices corresponding to either solely macro- or solely micro-scale systems.

2.2 Applications

Fouling resistant micro-filtration and analysis systems enable particulates in solution to be separated efficiently with minimal device contamination and extended device longevity. The separation of particulates in suspension can be used for many different purposes. Many of the applications noted throughout this paper encompass healthcare related devices. However, it is important to keep in mind the immense breadth of applications of filtration and separation technologies.

Micro-filtration methods, especially cross-flow micro-filtration, have been shown as viable separation techniques of biofluids and other suspensions traditionally separated via centrifugation (micro- or ultracentrifugation). For example, many protein suspensions, such as those in blood serum, are separated based upon relative densities in an ultracentrifuge [2]. Additionally, yeast and bacteria used in pharmacological industrial processes are often separated from their byproducts via centrifugation. Compared to highly selective and efficient filtration systems, centrifugation and other

separation techniques have limited applications. Conversely, the advancement of micro-filtration methods and advent of new micro-filtration methods can potentially address an extensive range of applications and result in numerous technological breakthroughs, while costing less and helping ameliorate economic and social inequities.

2.2.1 Reducing cost of and increasing availability of healthcare

While healthcare status quo of care is quite high in the western world, the US spent over 2.5 trillion dollars in 2009, which was about 17.6% of the Gross Domestic Product (GDP) at the time, one of the highest percentage of GDP for healthcare in the western world [6]. While the causality between the cost and benefit of health care is somewhat arguable, no logical reasoning exists against the development of technologies of equal or better efficacy that cost less. Furthermore, with the US and other western countries at the forefront of technology and medicine, actions in the US have significant influence worldwide. Unfortunately, the US standard of care is financially unattainable in many parts of the world. For these reasons, it is appropriate to investigate technologies of reduced cost. The materials, manufacturing methods, and theory behind this project were implemented with these low-cost goals in mind.

Because of the expense of modern health care technology, much of the world is insufficiently equipped and suffers from maladies nearly non-existent in the US. Infectious diseases remain the leading cause of death in developing countries [7]. The development of portable, low cost, high throughput devices that can isolate and identify pathogens or other disease markers or metabolic byproducts may provide incredible advancements in the diagnostic capabilities of low resource areas. Targeted areas often

lack the funding for decent equipment and personnel trained in their use. Simple, low-cost diagnostic tools may give those in affected areas the ability to run a range of tests without the assistance of highly trained staff. Many research groups have made note of the need for such low-cost devices in the US as well as in the developing world.

2.2.2 Municipal water purification

One other technology that arguably targets the source, rather than simply diagnosis, of infectious disease is efficient water filtration. In municipal water filtration systems, a large portion of the operational cost is due to filter fouling [5]. Clean drinking water is elemental to the advancement of the health of those in developing areas. These technologies could be implemented where little infrastructure exists, requiring little power and operational skill, but providing clean drinking water. In fact, the technology developed through this project may be scaled up to larger scale water purification systems for small communities.

2.2.3 Military applications

The threat of chemical and biological warfare agents has driven the need for portable, accurate, and inexpensive detection systems for the military [7]. However, almost all raw samples are complex solutions that require pretreatment, e.g., filtration, prior to assay. In military and other field applications, reusability and long-term functionality are of key importance. These technologies are applicable for small portable devices used in the field by military personnel.

2.2.4 Why are filters important in bioanalytical diagnostics?

Diagnostic equipment requires the separation of various species in aqueous media such that the target is available to be analyzed by the sensor. These targets may be cells,

proteins, hormones, and other biomarkers [8]. Recently, trends in diagnostic medicine have shown the importance of biomarkers and other cellular signals as evidence of a disease state. In the future, researchers say diagnostics technologies will likely move toward highly comprehensive testing, saving time and money, increasing accuracy, and expanding the scope of molecular diagnostic tools that we know today.

In order to obtain quality samples representative of the condition of the person sampled, separation and analysis techniques must not alter cells or proteins used in the analysis. Some separation techniques, such as centrifugation, may disrupt the membrane of cells or cause them to lyse. Many reagents involved in the sample preparation may have deleterious effects on the structure or nature to the biomarkers being tested. Methods that reduce the potential for unwanted sample contamination or modification are ideal aspects of sample pretreatment and separation protocol.

Diagnostic technologies are less regulated and arguably less advanced than therapeutic technologies. Currently, standards for diagnostic tests are less strict than those for therapeutic technologies. Consequently, diagnostic devices have not had the same pressures for advancement and standardization as therapeutic technologies. One research area that has become popular in the last two decades, known as evidence-based medicine encourages the use of technology based diagnosis rather than "soft" diagnosis based upon physician review of symptoms and physician experience, which is relatively qualitative and not necessarily consistent. Devices that aim to enhance the development of accurate, repeatable, quantifiable tests will benefit future of diagnostics.

2.3 Specific Uses

2.3.1 Cancer Diagnosis

High-sensitivity and high-throughput microfluidic devices may offer resolution necessary to detect cancer cells or biomarkers for early disease diagnosis. Researchers have observed trends that suggest biomarker detection may be more feasible in early stage tumor development [8]. Difficulties in the treatment of cancerous tumors can often be mediated by early detection and treatment. With the development of biomarker detection and analysis tools, researchers may be able to identify the tissue of origin and target that specific type of cancer and find less toxic cancer treatments that target early stage tumors. Biomarkers also have indications as to whether or not a cancer is malignant [8]. Esserman et al. suggests that one application could save some patients from being overtreated. If tumor tissue is analyzed after resection and determined not an aggressive phenotype, a patient may be spared unnecessary treatment, such as chemotherapy or radiation. The aggressive types of breast cancer, which have not seen the same decline as other types recently, must be detected early, likely before a tumor is large enough to be felt or even seen on a mammogram. Similar to other pathologies, in the future, concepts and techniques developed through this project could be applied to the detection of cancer through the sequestering of cancer cells, detection and quantification of biomarkers, as well as the general management and preparation of sample specimens. These detection techniques go back to the original intent of the project.

2.3.2 Portable Fouling Resistant Filtration

Significant motivation lies in the advancement of dialysis procedures. The most common schedule for a patient receiving dialysis treatments consists of appointments

lasting three to four hours three times per week or more [9]. Not only is this therapy time consuming and inconvenient, but also lacks efficacy, as those individuals on dialysis have significantly reduced life expectancies compared to healthy individuals [9]. As the core procedure behind dialysis is the removal of waste from the blood through ultrafiltration and fluid ion balances, the technologies investigated in this project are clearly applicable. Furthermore, the development of artificial kidney and spleen technologies could be benefited by such capabilities. For example, DEP based technologies could help separate viable and nonviable red blood cells and aid in the removal of toxins and waste, all through discrimination based on differences in permittivity and conductivity of different types of cells, live versus dead cells, or disease phenotype.

2.4 Traditional Methods for Fouling Resistant Filtration

Previous anti-fouling methods have included sample pretreatment, coagulants, and adsorbents, which increase cost, sludge (waste), and decrease flux, but decrease fouling [10]. One experiment using synthetic wastewater in an ultrafiltration system adapted to periodically relax, increase cross-flow velocities, or a combination of the two. Results showed a 30-minute production time followed by a 1-minute relaxation increased flux. A one-hour production time with cyclic 30 sec relaxation periods further increased flux. The mechanical and bulk methods of reducing filter clogging are effective but time consuming, and in some instances, stopping operation to relax or flush the system is not favorable or even possible [11].

Other traditional anti-fouling techniques include the addition of chemical, mechanical or ultrasonic perturbations, ideally causing particulate matter to keep from attaching or to detach from the membrane surface. These techniques include

backpulsing, air splurging, chemical pre-treatments, and chemical and biological cleansing protocols. However, all of these processes require stopped processes, external equipment, such as pumps, as well as possible damage to the filtration membrane itself. Furthermore, when handling potentially delicate biologics, chemical and biological agents may harm the species targeted for detection or analysis [10].

2.4.1 Cross-Flow Filtration

One of the most effective techniques currently used to alleviate filter fouling is known as cross-flow filtration. Contrary to a dead-end type filtration process, where the entire suspension if forced through the filter membrane via flow perpendicular to the membrane with no alternate path, usually by way of a pressure gradient, a cross-flow filtration system allows the suspension to flow over the membrane tangentially, allowing flow either through the filter membrane or an alternate retentate outflow [11]. In the case of the cross-flow design, particulate matter trapped by the membrane can be swept off the surface into the retentate collection vessel.

Adjustments can be made in order to optimize the flow rates and pressure gradient across the filter membrane such that the filter attains peak efficiency. However, the efficiency, meaning the volume of suspension processed during a finite period of time, is often lower in cross-flow filtration systems than dead-end filtration, as a large percentage of the suspension will bypass the filter membrane and be recirculated or simply collected in the retentate. Because only part of the suspension travels through the filtration membrane, the rest must be cycled back through the system to be "re-filtered." Although seemingly less efficient, when all other variables are assumed equal, cross-flow filtration can actually be more efficient compared to dead-end filtration, after accounting for the

negative effects of fouling. Cross-flow filtration is one of the techniques that will be used in this project to limit filter fouling.

2.5 Possible Biofluid Samples

2.5.1 Blood/Plasma

Blood is an incredible source for information about the entire body, as it is in contact with nearly all tissues [12]. Not only is blood a conveyor of oxygen, carbon dioxide, wastes, and metabolites, but also a tissue housing immune cells and their constituents. Most current blood analysis techniques require specialized equipment and trained personnel. Some of the basic hematological analyses include light microscopic evaluation via Wright-Giesma stained slides and manual cell counts by hemocytometer [13]. More recent technologies, offering higher throughput, include automated cell counting systems, such as the Coulter Counter and flow cytometry. To maintain accuracy, these technologies require trained personnel and highly controlled laboratory environments [12]. In addition, as with any process requiring manual handling, human error can cause artifacts that reduce the validity of such test results. For these reasons, the microfluidics research community seeks to develop new technologies requiring little user handling that can be used with whole blood or plasma.

2.5.2 Saliva

As a biofluid sample, saliva is advantageous over blood, as it is readily available and can be procured noninvasively. Saliva contains much of the same components as blood plasma and studies have shown the protein content in oral fluid is relevant to various disease biomarkers [14]. An experiment by Herr et al. used a microfluidic chip to test for periodontal disease, wherein the researchers performed on-chip gel

electrophoresis to isolate a type of matrix metalloproteinase (MMP) characteristic of the disease. These technologies are incredibly promising diagnostic tools for the developing world, where the invasive medical technology such as needles can exacerbate the spread of infectious diseases.

2.5.3 Sweat

Just like other biofluids, sweat contains factors and biomarkers that may be helpful in the diagnosis of disease. Other applications already being produced include sweat-based drug testing. The Cal Poly Biofluidics lab also has been working with the Department of Defense on sweat-based sensors for nefarious chemicals for military detection purposes.

2.6 Dielectrophoresis

The physical phenomena of electrophoresis (EP) and dielectrophoresis (DEP) have been used extensively in the manipulation and separation of particles. While electrophoresis is a commonly known process, namely because of the highly valuable processes of Polymerase Chain Reaction (PCR) and gel electrophoresis, DEP is a lesser known, but highly researched tool as well. DEP was first defined by Pohl as the translational motion of a neutral particle due to an inhomogeneous electric field [15]. Because DEP can be used to manipulate neutral particles, it is applied much differently than EP. The direction of the induced force (positive or negative) depends on the relative permittivies of the particulates relative to the solvent, as well as the frequency of the applied potential [1].

2.6.1 Dielectrophoresis Theory and Expressions

DEP is not an intuitive electric field phenomenon, compared to EP, where fundamental "opposites attract" reasoning is sufficient for a basic understanding. Mathematically, DEP is a second-order electro-kinetic phenomenon. While the expression for EP is dependent upon electrical charge, the DEP expression is dependent polarizability (the ability to induce a dipole) [16]. Once the dipole is induced in an electric field, the Columbic (electrostatic) forces on the particle are only balanced if the electric field strength is equal on both sides of the particle. Consider the following illustration, Figure 1, which demonstrates how the unbalanced field causes a corresponding nonzero sum of forces.

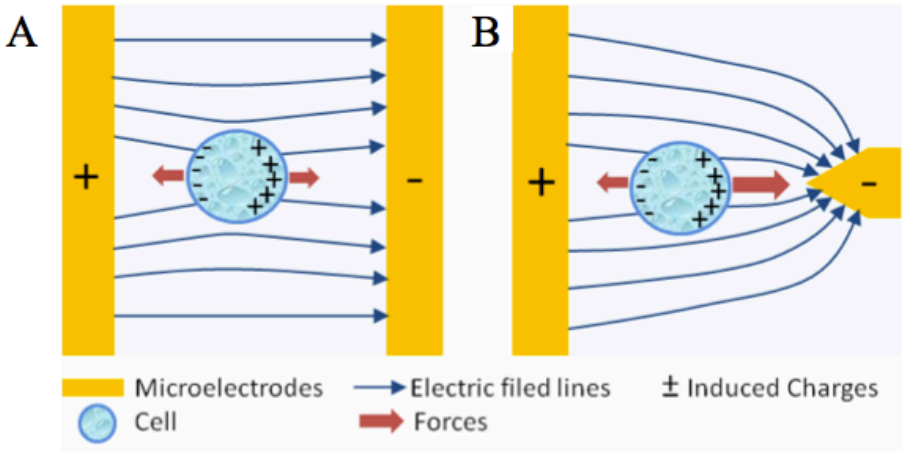

Figure 1 -- Illustration showing the difference in the electrostatic forces on cells or particles in equal (A) versus unequal (B) electric fields (Adapted from [17]).

In any polarizable particle in any electric field (uniform or non-uniform), a separation of charges will occur. In the uniform field (*A*) in Figure 1, the electric field interacts equally and oppositely on either side of the particle. However, in the non-uniform filed (*B*), the strength of the electric field is significantly different on either side

of the particle. This difference results in an unbalanced electrostatic force. Eqn. (1) shows the basic electrostatic force relationship, where *F, E,* and *q* refer to the force, electric field, and charge density, respectively.

$$\boldsymbol{F} = \boldsymbol{E}q \tag{1}$$

In a uniform electric field (as seen in *A* of Figure 1), the sum of the force vectors from Eqn. (1) above is zero. However, in an inhomogeneous electric field (*B* in Figure 1), the electric field strength on one side of the particle is different that the other, resulting in a non-zero sum of forces.

For an electric field to be inhomogeneous from the perspective of a particle, the relative size difference of the particle to the non-uniformity in the field dictates whether or not DEP behavior can be elicited. In other words, the field has to be significantly different (and magnitudes of field strength high enough) for any forces to develop. Thus, the gradient of the field (amount that the field is changing) is a main predictor of the magnitude of the resultant force. For reasons discussed later in this section, the size of the particle is the second predictor to the force elicited, which makes DEP an especially powerful tool for size based separations of particles on the micron size range.

While the previous two variables affect the **magnitude** of the force produced on a particle, the polarizability of the particulate relative to the polarizability of solvent determines the **direction** of the force. An expression, known as the Clausius-Mossotti factor, as seen in Eq. (2) compares the complex permittivities of the particle and solvent.

$$f_{CM} = \frac{\varepsilon_p^* - \varepsilon_f^*}{\varepsilon_p^* + 2\varepsilon_f^*} \quad \textbf{(2)}$$

where,

The subscripts *p* and *f* indicate particle and fluid, respectively.

ε = relative permittivity (farads/meter)

* indicates complex number

The complex relative permittivity is defined as follows in Eq. (3).

$$\varepsilon_i^* = \varepsilon_i - \frac{j\sigma_i}{\omega} \quad \textbf{(3)}$$

where,

$$j = \sqrt{-1}$$

ω = the driving frequency of the applied potential

i = placeholder for the i^{th} substance (particle or solvent)

According to Eqn. (2), if the particle permittivity is larger than the fluid permittivity, the Clausius-Mossotti factor is positive. Alternatively, if the particle permittivity of is lower than that of the fluid, the Clausius-Mossotti factor is negative. Because this factor is multiplied into the general force expression for DEP (Eqn. (4), below), the resultant sign dictates the direction of the induced force.

According to Pohl, "dielectrophoresis depends upon the square of the electric field intensity…because the polarization producing the dipole depends upon the field strength to the first power, but the response of the dipole to the field gradient" [15]. Pohl provides the following general equation, Eq. (4), for the force generated through a DEP field on a small spherical particle.

$$F_{DEP} = 2\pi a^3 \varepsilon_f Re\left[\frac{\varepsilon_p^* - \varepsilon_f^*}{\varepsilon_p^* + 2\varepsilon_f^*}\right]\nabla|E|^2 \quad \textbf{(4)}$$

where,

ε = permittivity (farads/meter)

Re indicates the real part of the Clausius-Mossotti factor

E = electric field strength (Volts/meter)

The equation shows the force experienced by the particle is proportional to the radius of the particle cubed and the square of the gradient of the electric field. Depending on the sign of the Clausius-Mossotti factor, the force will be either positive (attraction, as particle will move from low to high electric field gradient) or negative (repulsion, as particle will move from high to low electric field gradient) [1].

Because the Clausius-Mossotti factor is complex and frequency dependent, the physical properties of the particle and solvent are not the only variables contributing to sign of the term. In fact, the frequency dependence allows researcher to "tune" AC DEP systems by adjusting the frequency of the source voltage. In other words, many systems are designed to have a specific "crossover" frequency, where the Clausius-Mossotti factor changes sign. In other words, the force produced on the particulate could be intentionally

changed from repulsive to attractive, or vise-versa, depending on the needs of the work being performed.

2.6.2 Many uses of DEP

In addition to the repulsion, attraction, localization, or separation of particulates, DEP research shows it capable other applications, especially biosensors. The following figure, Figure 2, shows the response of a typical mammalian cell to DEP fields according to the applied field frequency. While the curve depicts the sign of the induced force (*y-axis*), the text in the figure introduces other information that can be parceled out from the cellular or particulate response. The article by Pethig et al. [18] discusses the potential for DEP in the characterization of stem cells, showing DEP response at lower driving frequencies reveal information on cell size and shape, cytoplasmic membrane integrity, and other morphological characteristics. Alternatively, at higher frequencies, other information, such as cytoplasmic conductivity and nucleus-cytoplasm volume can be gathered. Because a cell will experience transition from negative DEP to positive DEP at a certain frequency, and said transition is dependent on cell morphology, researchers can identify cells and obtain morphological information by observing at what exact frequency the transition takes place. In addition, properties such as cytoplasm conductivity can be assessed because the plasma membrane, essentially a capacitor, is shorted at high frequencies.

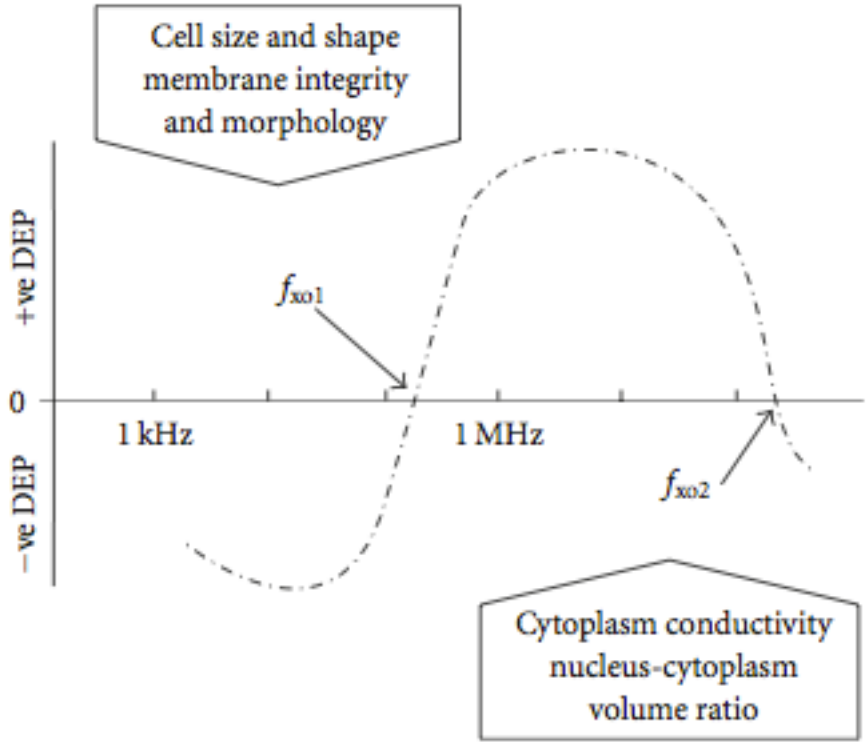

Figure 2 -- Changing the frequency of the applied field results in changes in the DEP response in cells. Note the two labeled "crossover" frequencies, where the induced force reverses direction (Adapted from [18]).

2.6.3 AC DEP

As seen above, DEP devices can use techniques not only to translate particulates or cells, but also to make assessments, all in one. This flexibility and breadth of functions has contributed to its popularity among researchers performing particulate related manipulations, whether for simple separations or highly sensitive biosensors. The preceding paragraph discussed the importance of the applied field frequency; for this reason, alternative current (AC) has traditionally been used for DEP fields. The nature of AC fields lends easily to the generation of non-uniform patterns and allows for the user to tailor responses via frequency adjustments. Before introducing the DC electric field methods used in this thesis work, it is important to note common electrode methods, which generally utilize AC fields.

2.6.4 Electrodes for Dielectrophoresis

The design of devices such that an inhomogeneous electric field can be produced is not trivial. The modern fabrication of electrodes for AC DEP fields often involves microfabrication technology to produce microarrays of electrodes [19]. Traditionally, complex geometries are needed in order to create the DEP field. However, as low cost and straightforward manufacturing is an important goal in this project, micro-patterned electrodes will not be used. The complex fabrication of these patterned electrodes often constrains DEP technologies into a category of higher cost and complexity of fabrication. For example, Choi et al. developed trapezoidal micro-patterned surface electrodes that were used to create DEP fields, but noted that the complex fabrication processes needed to fabricate these electrodes proved a significant and real disadvantage [20].

Complex fabrication techniques for the development of the desired electric field are not solely limited to the electrodes. Many of the regimes for generating DEP forces in microfluidic and other devices entail complex, spatially non-uniform channels and features. While some inhomogeneous fields are generated because of the geometry of the electrodes, others have used insulating posts to make an otherwise uniform electric field non-uniform. These insulative features "bend" the electric field lines, thus making the field non-uniform and allowing for a DEP field to develop, affecting the trajectory of the particles, as seen in Figure 3 [21].

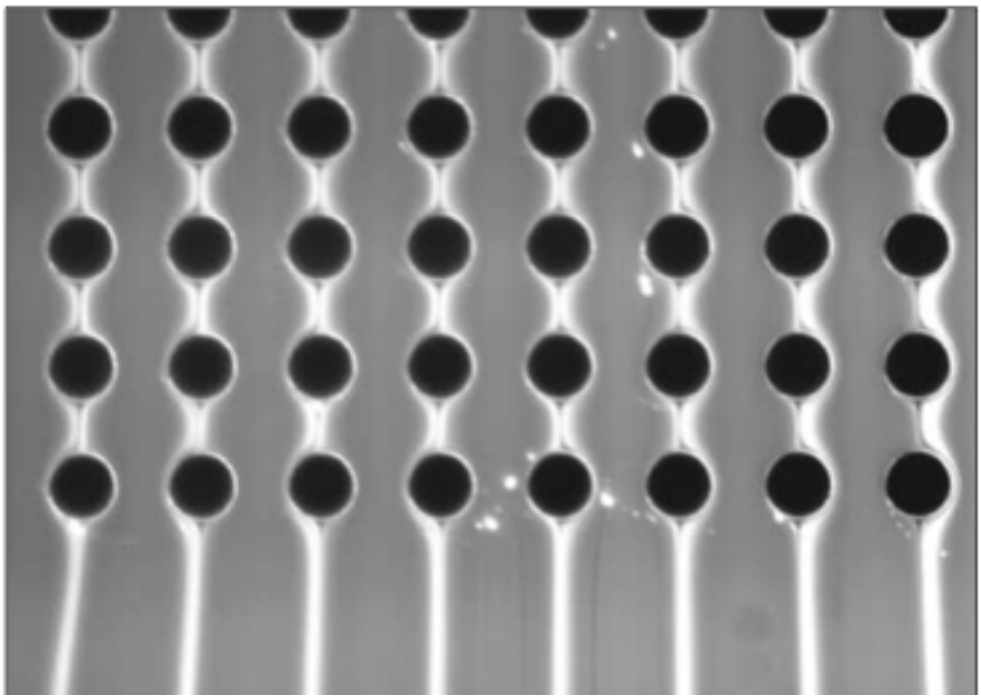

Figure 3 -- Image of fluorescent bead flow through array of 33 μm diameter insulative posts (63 μm spacing center-to-center) in applied field of 25 V/mm. The particles used in this experiment experience *negative* DEP and displaced away from the posts [21].

2.6.5 AC DEP Disadvantages

While AC DEP has many benefits, it is limited by cost. Fabricating the complex patterned electrodes needed for this technology is difficult and expensive, especially for a

one-of-a-kind prototype. For this reason, we have decided to move past AC DEP and explore a DC DEP as a less expensive means that relies more on inherent properties of the particles and solvent. Through the manipulation of other factors, we can tailor our DC field to elicit the repulsion of particles away from the filtration membrane and enhance the filtration.

Critical aspects of the design took advantage of the intrinsic properties of the filter membrane and a straightforward, but novel, electrode design to elicit the appropriate electric field characteristics. Because of this design, we were able create a much less expensive device than many other DEP based prototypes. The development of the theory for DC DEP on our platform follows immediately and the aforementioned electrode design and fabrication will be discussed further in the Materials and Methods section.

2.6.6 DC DEP Theory and Development of Device Mechanics

In order to establish the DEP relationship with a DC applied potential, the previously introduced general equations must be simplified. Because the frequency of the DC field is zero, simplification of Eqn. (2) transforms the real segment Clausius-Mossotti factor into an expression solely dependent on the conductivities of the particle and solution.

$$f_{CM} = \frac{\sigma_p - \sigma_f}{\sigma_p + 2\sigma_f} \quad \textbf{(5)}$$

With this simplification of the Clausius-Mossotti factor, we establish a DEP equation for suspensions in DC electric fields, Eqn. (6).

$$F_{DEP} = 2\pi a^3 \varepsilon_f \left[\frac{\sigma_p - \sigma_f}{\sigma_p + 2\sigma_f} \right] \nabla |E|^2 \quad \textbf{(6)}$$

As separation via filtration is based upon flow, the hydrodynamics of the device are equally important as any DEP repulsions or other manipulations. We know from fundamental fluid dynamics that the hydrodynamic force on a spherical object in a Newtonian fluid can be described as follows in Eq. (7).

$$F_{\mu} = 6\pi a \mu U_{ave} \quad \textbf{(7)}$$

where,

F_{μ} = hydrodynamic (viscous) force

a = particle radius

μ = viscosity

U_{ave} = average velocity of particle

Depending on the properties and setup of the device, the DEP forces could either be opposing or enhancing the viscous forces. Depending on the average fluid flow, viscosity of the media, permittivities of the particles and media, and the electric field gradient, the DEP force has the potential to overcome the bulk flow. As one of the primary experimental goals of this project is to use DC DEP to reduce or eliminate clogging of the filter membrane, we can equate these equations to predict if the DEP

force can be used to repel or levitate (balance of forces) the particles above the filter surface. This levitation is mathematically implemented by setting Eqs. (6) and (7) equal to one another as shown below in Eq. (8).

$$F_H + F_{DEP} = 0$$

$$F_H = -F_{DEP}$$

$$6\pi a \mu U_{ave} = -2\pi a^3 \varepsilon_f \left(\frac{\sigma_p - \sigma_f}{\sigma_p + 2\sigma_f}\right) \nabla |E|^2 \quad \textbf{(8)}$$

If all other terms are known or assumed, this equation can be used to determine electric field characteristics that cause particles to remain suspended normal to the plane of the electrodes. While this phenomenon may be employed to move one type of particulate in an aqueous solution toward or away from the electrodes, more difficult is the separation of two different types of particles in suspension. DEP excels in these complex separations, as species with different dieletric properties will experience distinctly different forces, and may be moved at different velocities or to differing areas of a device. The major difference that can be exploited in this setup is differences in size, as the radius term is a cubic. Hence, small differences in the diameter of particulates should result in relatively large difference in the DEP force on the each particle.

Using the separation of whole blood as an example, we can put this theory into perspective. Suppose we are interested in separating red blood cells from plasma proteins and platelets. The average diameter of a red blood cell is 7.2 μm, while mature platelets have an average diameter of 2- 4 μm [13]. By cubing the radii of each (assume the average diameter of a sample of platelets is 3 μm), we find that the average red blood

cell will experience 13.82 times the DEP force than the average platelet. Although this particular comparison does not take into account the increased hydrodynamic drag of the larger red blood cell which will reduce the speed of its repulsion, this comparison illustates the large relative forces that can be generated, all on a physiologic and diagnostic appropriate range of diameters. Following this separation, downstream operations could also be assisted by DEP as well, the only difference being the sizes of the particles separated will became smaller and smaller . For instance, the same principle can be used to separate platelets from plasma proteins (nanometer size range), all performed with reduced filter fouling, resulting in longer filtration membrane life, lower pressures, and more accuracy and specificity.

2.7 Current Research in DEP Separations

As mentioned earlier, most current DEP separator techniques today use AC fields, so much of the literature researched in this project involved AC DEP. The experiment performed by Du used a pulsed AC DEP signal and insulated electrodes. They determined a critical frequency of 200 kHz at 200 V, which resulted in a charge density of 160 V/mm. They used 0.5 mm diameter wire for the electrodes and a 0.25 nm thick plastic film to insulate the electrodes. The particle size distribution in their suspension was 100 to 3000 nm. They fed the suspension at 40 L/(min m^2) over a filter area of 2.84e-3 m^2 with an opening of 34 mm^2. In this case, the particle diameters were much greater than the average pore diameter of the membrane. The least amount of fouling was seen when the DEP signal was pulsed on and off [10].

With non-charged colloids, it is possible for dielectrophoretic motion to elicit higher velocities than electrophoretic motion (electrophoresis) of similar charged species.

In one study, using DEP via an AC signal, particles were levitated above a membrane. The colloids consisted of latex particles 1-2 micron diameter and 50-micron wide electrodes alternated with 50-micron gaps. The signal given to the electrodes was 50-75 volts at 10 – 600 hertz. They performed finite element analysis (FEA) of the DEP forces, which showed that the particles could be levitated at a height of two times the electrode width, meaning that, depending upon the magnitude of the hydrodynamic forces, the latex colloids could be equally and oppositely balanced by the DEP force [1]. Thus, the particles were able to flow over the membrane at said height without interacting with the membrane and causing fouling.

Researcher Hwang et al. [22] determined interesting trends in filter flux and "cake formation" related to flow rates and pore size. Using PMMA particles of average diameter 0.15 micron and density of 1210 kg/m^3, they determined two novel results. First, if the pore is too large relative to the colloid, there is an increased chance of "cake formation," as it is hypothesized that when multiple colloids can fit into one pore at a time, they are more likely to become stuck in that pore. Similarly, at lower flow rates, the "cake formation" can become more likely, presumably because there is a higher change of colloid-filter interaction at low velocities. So, in a certain range, as flow is increased, the chance of clogging decreases. Under the same flow conditions, using the 0.15 micron beads and two filter membranes with 2 micron and 4 micron pores, respectively, the researchers found the 4 micron clogs first, as seen in Figure 4.

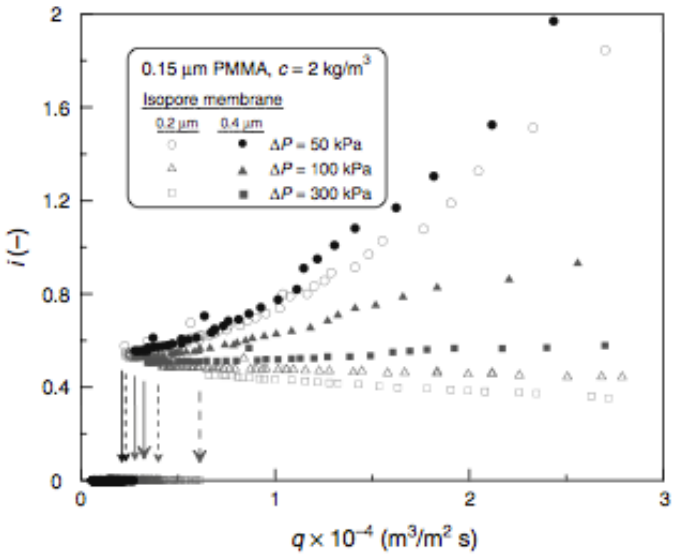

Figure 4 – Chart of the flow versus i(-), a dimensionless representation of the degree of cake formation. Note that, at all pressures, the 0.4 μm pore membrane experiences greater cake formation [22].

However, Hong et al [23] have shown the agreement of theoretical predictions and experimental results pertaining to the effects of solute concentration in the feed suspension on the cake layer formations. Their experiment also elucidated on the effects of high pressure on cake formation. Not only did they find larger pressure gradients were correlated with accelerated cake formation, but also the cake itself was thicker and denser, and thus more resistant to flow.

Much other research related to various aspects of filter membranes has been performed recently. Some of this research has included the modification of filter membranes and pores in order to change properties such as hydrophobicity or hydrophilicity. Some of the literature reports to chemically treat filter membranes in order to produce electrochemical sensors. In this particular study, researchers modified a polyethersulfone ultrafiltration membrane with an average pore size of 10 nm with three additive films. The purpose of these films, which were a 20-micron film of gold, a

NiTSP film, and a Nafion film, were to increase the transport of Li+ ions through the membrane. They characterized the porosity with an atomic force microscope (AFM) and found a decrease in surface porosity, but determined that the permeability of Li+ had increased, suggesting that the coating facilitated the transport of the ion [24].

2.7.1 Fluid Properties

As the DEP force is interrelated with the fluid permittivity and conductivity, the electrical conductivity (i.e. concentration of salts) of the media can vastly affect the dielectric value of the particles [15]. In fact, Pohl states that species that actively interact with surface of the colloid greatly increase the dielectric constant of the colloid, as seen in an experiment with 5X10^-5 M Na_2CO_3 and glass beads. Thus, the composition of the buffer or solvent can vastly affect the DEP properties.

In research presented by Wang, buffer was prepared with 8.5% (w/v) sucrose and 0.3% (w/v) dextrose. Conductivity was targeted to 10 mS/m by adding small amounts of EDTA (adjusted to a pH of 7.0 with NaOH) with a final pH of buffer being about 6.8. In a similar experiment, Kang et al [25] used a 10^-3 M Sodium Bicarbonate (Na_2CO_3/$NaHCO_3$) buffer and non-conducting particles. Of course, other fluid properties besides ionic concentration and conductivity, such as viscosity, will affect the performance of any particle separation, but likely contributes to a lesser extent.

2.7.2 Microparticle Properties

Most of the microbeads or microparticles that are used in experiments related to microfiltration are manufactured from various polymer plastics. The manufacturers attempt to minimize the variation in diameter among microbeads of the same type. Some of the common materials used for microbeads include polystyrene, latex, silica, and glass

[15, 22, 26]. While the properties of synthetic particulates are highly different than cellular characteristics, polymer beads are a valid approximation in DC DEP because the Clausius-Mosotti factor is only dependent upon conductivities, not permittivities. In other words, most cells and the synthetic polymer beads used in this work can be safely and similarly categorized as nonconductive particles, both having conductivities several orders of magnitude lesser than aqueous solvents. Polymer-based microbeads are very common in the literature and much research has been performed using many different types, including colored, fluorescently tagged, surface modified, and unmodified microbeads. The type of microbead may affect the dielectric properties of the bead, and thus affect the separation or filtration of a suspension made with that bead. However, the type of microbead, is also largely dependent upon the methods for validation, as the number, concentration, or location of the bead must be determined experimentally. The following section covers some of the more common detection and validation techniques used in the field.

2.7.3 Detection and Validation Techniques

Most of the researchers have experimentally validated the effectiveness of filters and other DEP separation devices with microbeads in conjunction with visualization tools, such that they are able to observe the flow paths of the respective target species. These setups include the relatively simple fluorescently tagged beads visualized with a video microscope recorded by a charge coupled device (CCD) camera. Others have used flow cytometry to count and characterize colloids, as that technology is capable of counting and sizing of particles. In fact, the Calibrite™ particles from Beckton Dickinson™ are used to calibrate flow cytometers.

Others have used ultraviolet (UV) detectors to count, locate, and size microbeads. In research presented by Wang et al. [19], UV light (254 nm wavelength) can be used with an optical sensor that responds to the attenuation of light by particles passing through the detector channel and causes a change in output voltage. The voltage output channel magnitude varies with the size of the colloid and can be charted in order to locate exact sensing time points.

2.7.4 Summary

Using the above research into the background, applications, physics and mechanics, and survey of filtration technologies, a DC DEP anti-fouling filtration system was developed. Many needs have been identified and the applications of technologies related to those presented are diverse, even within the realm of biomedical engineering and biotechnology, spanning from microfluidic diagnostics to industrial processing of biopharmaceuticals. The theory presented thus far gives justification toward the technical basis of the project and will be elaborated further in the final section of the background, where software modeling utilized to describe the mechanics of the filtration is presented. The following chapters outline the rest of the project from design development and fabrication through experimental validations and conclusions on the current validity and future possibilities of this approach.

2.8 COMSOL™ Models: Electric Field Through Filter Pore and Hydrodynamics

As the device design was being developed, a COMSOL™ model of a simplified electric field was developed to validate our design ideas. In this model, the electric field of a single filter pore was modeled. The model had boundary conditions and subdomain

properties derived from the material properties of those used in the device. The main difference is only one pore was modeled, as opposed to the 5-20% porosity [27] of the actual filter membranes. The overall geometry was not exactly replicated, as the model is two-dimensional, but it was scaled appropriately. The potential source is the upper active electrode, which is located in the upper domain of conductive media. The subdomain of the pore (in Figure 5, the pore is where the electric field lines end in a sharp point) also has conductive fluid. The rest of the filter membrane is non-conductive (see the flat line on the graph). The subdomain below the filter membrane is also conductive fluid, such that the electric field lines run from the top charged electrode and curve downward through the pore (high gradient) and through the bottom subdomain to the ground bottom electrode.

The equation for electric field gradient was added to the *Cross-Section Plot Parameters* (within the *Post Processing* menu) expression for line plots in COMSOL™ and displayed in the graph (Figure 6), which shows the electric field gradient over the (contiguous) non-conductive filter (flat line) and large negative spike over the pore area. The highly negative gradient value at the pore is expected and helps to validate this design, indicating the field does have a large negative gradient through the pore. The following graph, Figure 8, shows the electric field gradient values found through COMSOL™ to estimate the speed that 10 μm particles may be repelled. While this model has some assumptions and simplifications, the results for the speed fall within the limits of reason on the range of millimeters per second at expected potentials in DC

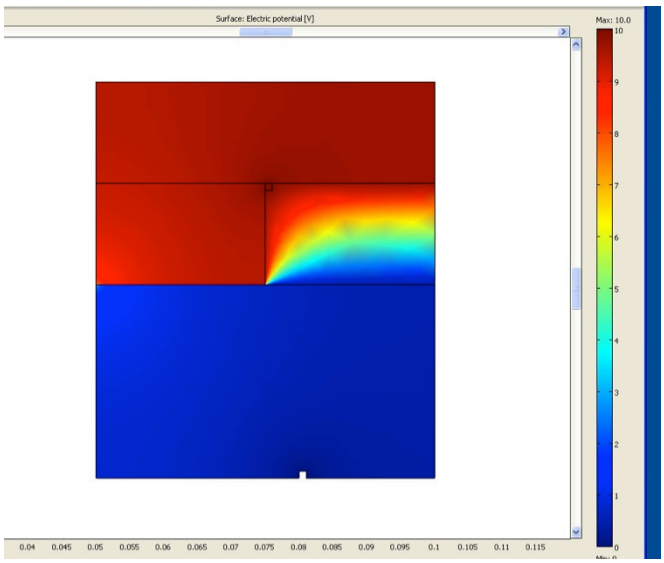

Figure 5 -- COMSOL™ representation of electric field through pore.

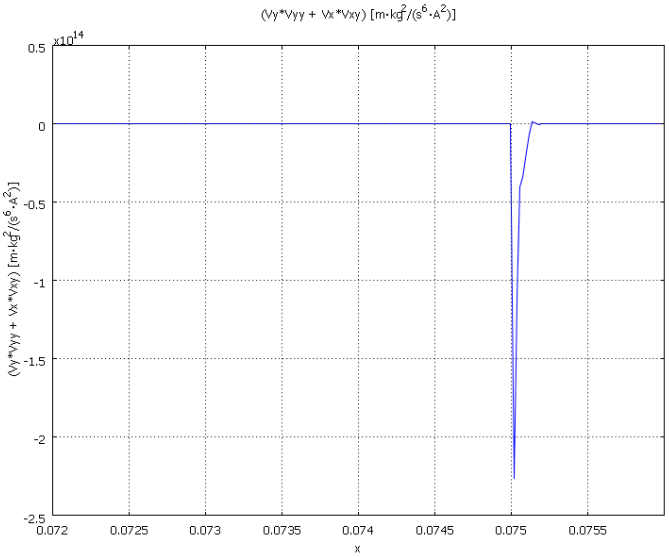

Figure 6 -- COMSOL™ plot of electric field gradient through pore.

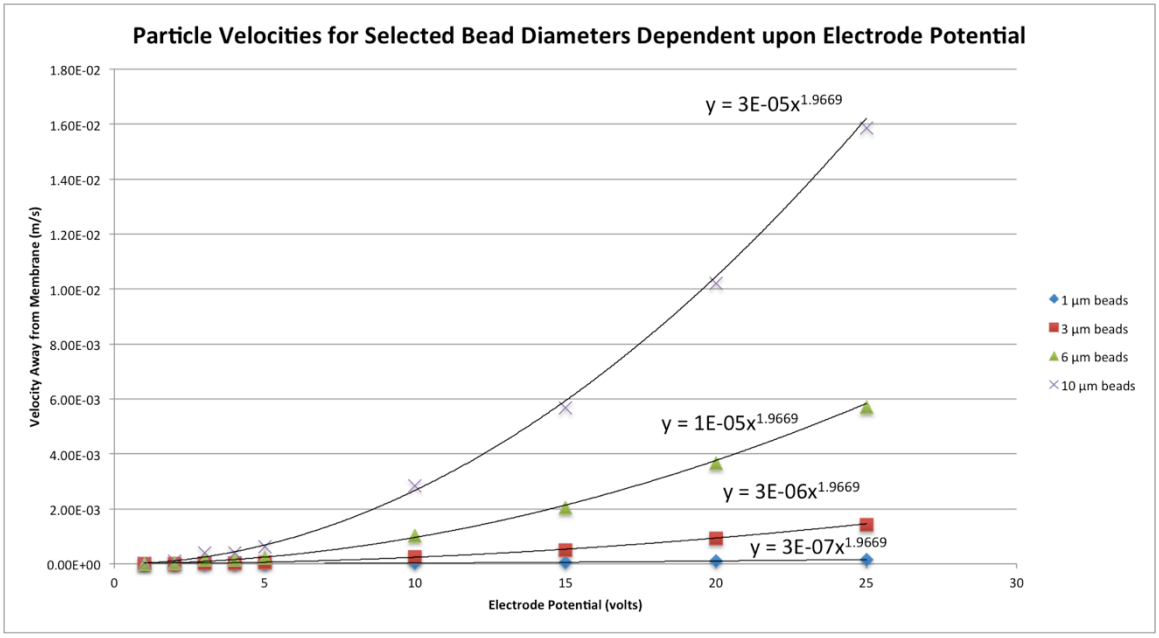

Figure 7 -- Expected velocity of sphere due to DEP force using COMSOL™ calculations. This representation assumes no external fluid flow, but shows particle motion resulting from DEP force.

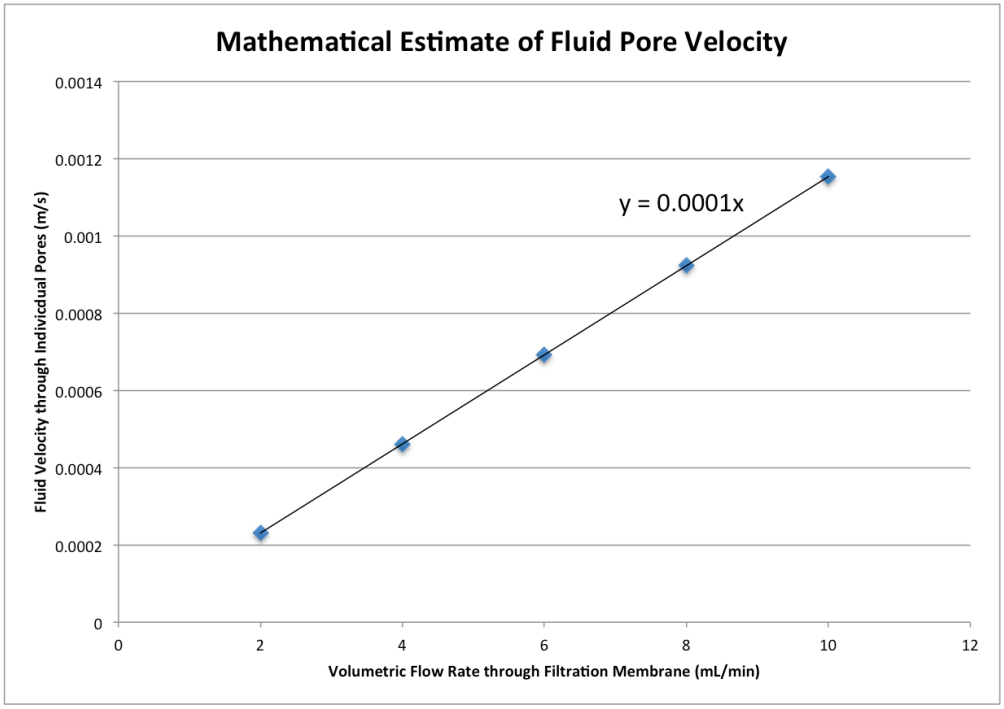

Figure 8 -- Graph shows the theoretical calculation of expected particle velocity through pore with no electric field present.

By combining the equations of the two previous graphs (Figure 7 and Figure 8) the following chart (Figure 9) was developed. By equating the estimated speeds (opposite velocities) imparted on the particles via DEP force and hydrodynamic force, the curve below shows the relative voltage necessary to levitate the particles versus the total inflow into the device. It is expected that the DEP force above the curve should be larger than the hydrodynamic force, resulting in fewer particles passing through the membrane. Correspondingly, in the area below the curve, the hydrodynamic force will outweigh the DEP force and particles will remain passing through the filtration membrane.

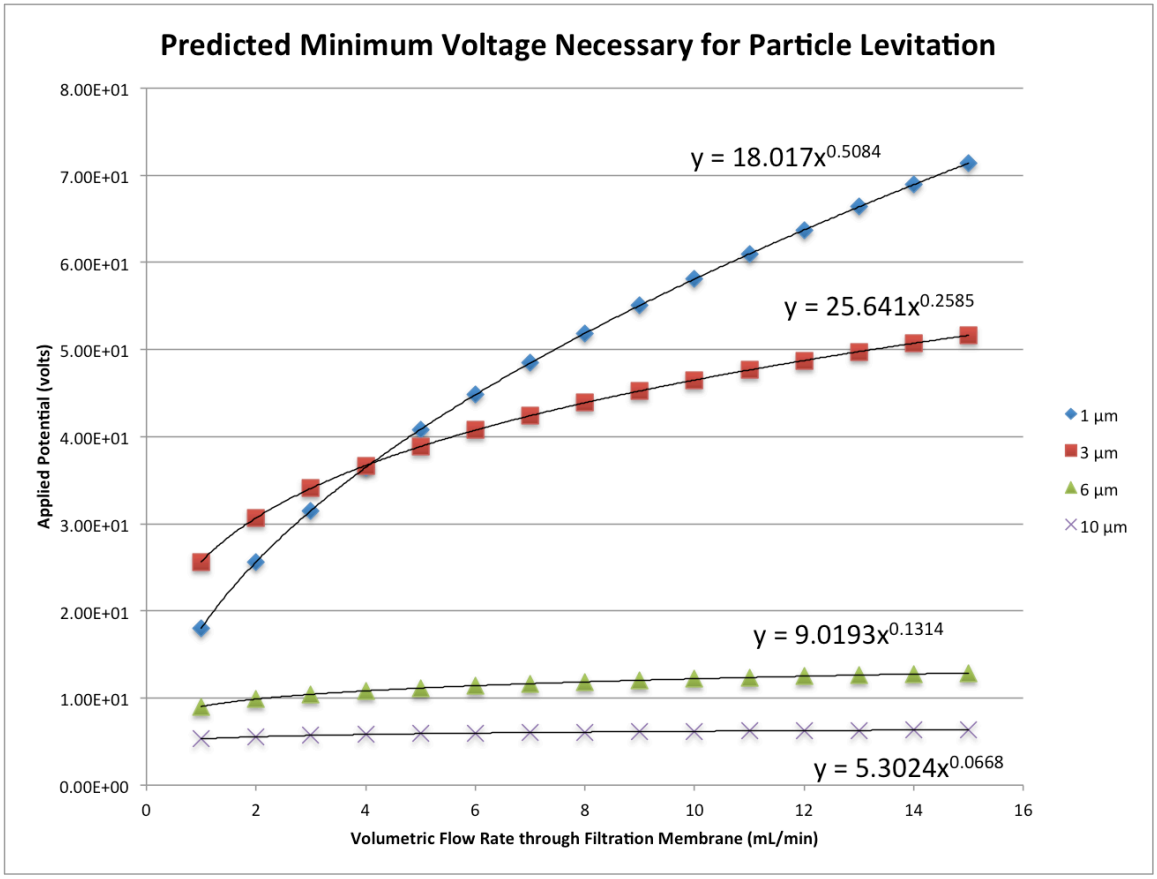

Figure 9 -- Graph shows the calculated minimum voltage necessary to levitate particles above the filter membrane. This is essentially a graphical representation of Eq. (8), using the COMSOL™ and calculated values, such that the particle velocity is zero (levitation) along the trend lines.

Consult Appendix A to further review the mathematics behind balancing the hydrodynamic and DEP for a more detailed description of the calculations that make up the preceding charts.

Other important flow conditions in addition to the DEP and hydrodynamic forces in the design of the device and the experimental validation is the residence time, the time for a complete "turnover" of fluid on the inflow side of the filtration chamber and pressures required to generate such conditions. While much of the design development that follows was motivated by the geometric constraints of the device, designed for adequate flow conditions is equally important.

Finally, the fluid velocity calculation above in Figure 8 was calculated via a simple volumetric fluid flow divided by void area of the filtration membrane (details shown in Appendix A Table 12). In addition, a COMSOL™ model shows the expected flow patterns through the device, as seen below in Figure 10.

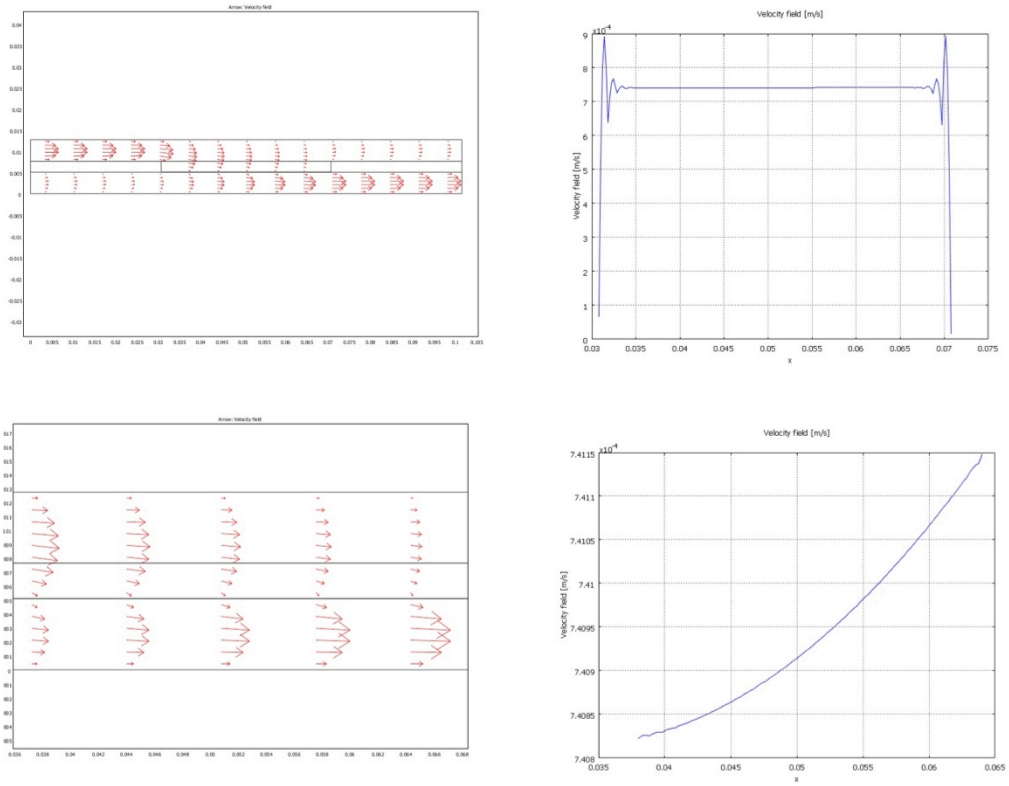

Figure 10 –The above charts show the COMSOL™ results for an approximation of the fluid flow in 2-D. The left charts show the flow through the device pictorially and the right side shows the corresponding flow through the membrane.

The top two images of the figure above show a 2-D representation of the device, such that the filter area is in the center of each image. This model confirmed our expected fluid flow across and through the filtration membrane, with the retentate and filtrate exit ports. As a major milestone of the project was to create the housing and foundation of the device (all before any DEP fields were applied), confirming appropriate flow paths and velocity approximations was essential. The lower images are simply enlarged subsets of the filter portion of the images. Note the velocity through the membrane increases as the flow moves away from the entry port. Graphically, this increase in velocity looks significant, but the numerical values actually increase very little.

3 Materials and Methods

3.1 Design Development

At the outset of the project, we performed research to assess the appropriate scope and goals. Several meetings with the advisor helped identify the expectations of the project, from software models through device fabrication and validation. The following two tables, **Table 1** and **Table 2** are adaptations from these discussions and included to describe the scope of the project.

Table 1 – Summary of task and deliverables adapted from a project planning presentation to help determine the scope of the project.

Includes	**Does Not Include**
Design models (Solidworks™ , AutoCAD™ , COMSOL™ , MATLAB™ & Microsoft Excel™ for calculations and data analysis)	An extensive COMSOL™ model
Design of device using commercially available filtration membrane	Design of filtration membrane
Fabrication of device using capabilities of Cal Poly machine shops and laboratories	Development of novel manufacturing techniques or third party fabrication
Design of experiments using capabilities of Cal Poly Biomedical Engineering department	Development of novel design of experiments

Includes	Does Not Include
Execution of validating experiments using food dye and synthetic particles in suspension	Experimentation with applicable biologic colloids (e.g., yeast or whole blood)

Table 2, as presented below, focuses on goals specifically related to the device itself. These constraints form the framework from which the design was developed. These conditions were checked as each iteration of the initial design was formulated.

Table 2 -- Specific goals of device design and manufacturing.

Includes	Does Not Include
• Final design • Low-cost manufacturing techniques, notably electrodes • Cut stock materials with laser cutter and mill • Bond and/or assemble parts • Attach electrodes, fasteners, and accessories (tubing and electrical connections)	• Manufacture of filter membrane or chemical or other alteration thereof • Complex high-cost manufacturing techniques such as injection molding or patterned electrodes • Design for mass production

From the outset of the project, the Millipore™ membranes used in the device were selected as the most appropriate filtration membranes. In some ways, the filtration membrane constrained the geometry of the device designs, as the membrane is circular

with a diameter of 47 mm. At some points in the design development, alteration of the filtration membrane was considered, in order to fulfill the requirements of other design geometries. Some of these ideas may have been possible by cutting the membrane on the LASER cutter. However, cutting polycarbonate, the material from which the membrane is manufactured, is not allowed, due to the toxic by-products produced. In any case, manipulation of the membranes would be difficult and time consuming and there would likely be little benefit so most designs were conceived with a 47 mm diameter filtration membrane as the basis of the design.

One such initial conceptual design housed the filtration membrane by sandwiching it in between two circular acrylic discs of acrylic plastic as seen in Figure 11 and Figure 12. The suspension inflow port could be machined into one side of the device, while the opposite end can have outflow ports for the retentate and permeate. Circular O-ring style gaskets may be used to form a seal between the mating pieces.

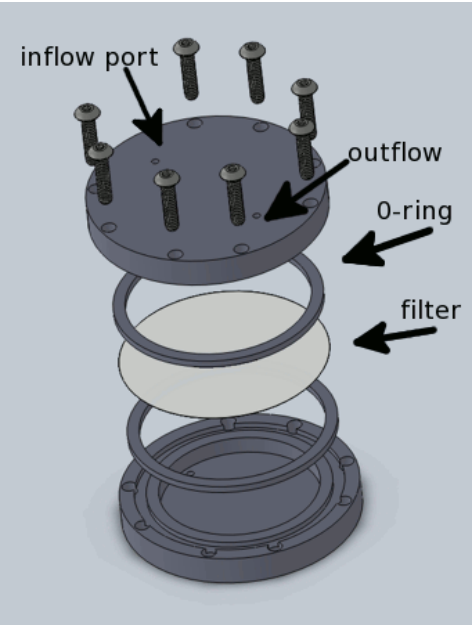

Figure 11 -- Solidworks™ sketch of one initial model in exploded view.

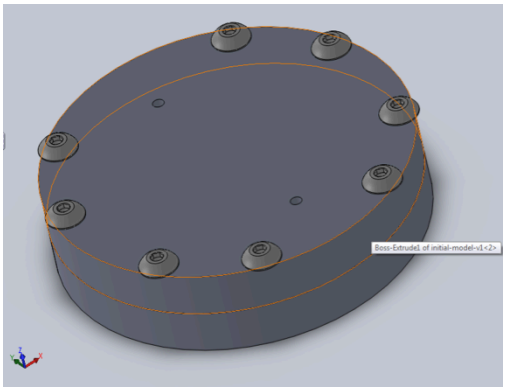

Figure 12 -- Collapsed view of initial model.

Several permutations to the design of the device housing were developed. The major divergence where the design changed from its conceptual model to that of the final design was changing from a two-part to a three-part assembly. For example, the initial design above has two major pieces needing fabrication, a top and bottom of a circular chamber having the necessary fasteners and fluidic ports. However, after considering many fabrication challenges, the design focuses transition toward a three-part assembly. In this case, the top, middle, and bottom pieces function as a top cover, flow and filtration channels, and a bottom cover. In the process of developing the general three-part design track, one model having two middle pieces was explored. This method, because of its complexity and redundancy was streamlined into an assembly of fewer parts, but ultimately was an influential iteration of the design development.

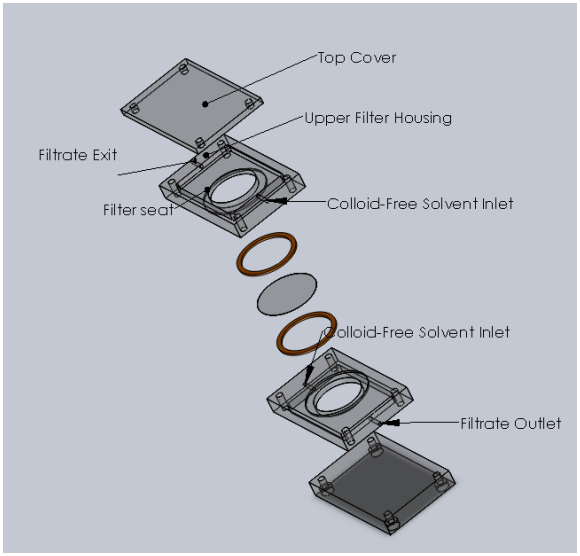

Figure 13 -- Conceptual model of assembly with two middle pieces.

This initial model was clearly not sufficient, as the filter securement and flow paths were not explicitly developed, but this generation helped visualize possible assemblies and basic geometries. These iterations were especially helpful in cultivating design ideas for washers and gaskets, as well as determining how to best secure the filtration membrane inside the device. For example, the following assembly, Figure 14, shows some of the initial gasket design and shaping of the inside of the chamber, such as the triangular expansions from the inlet ports.

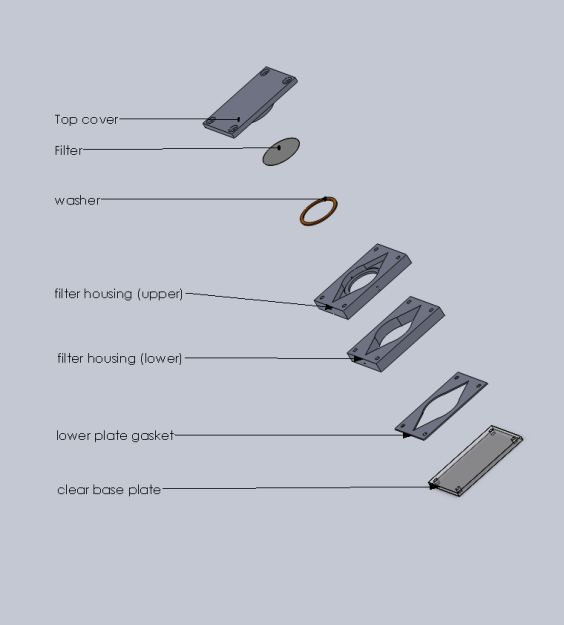

Figure 14 -- Second iteration of four-part design. At this point, geometries of the final design are established

The design of the middle part or parts prior to this point would have likely led to difficult and ineffective assemblies and overall performance. Because this device is a fluidic chamber, each additional joint or part increases the likelihood of leakage. This issue encouraged the development of a more condensed and simplified design, having fewer areas vulnerable to misalignment and leakage. This shift in the design as seen in Figure 15 was the last major change in the overall concept. Key components, such as the filter stabilization arms (Figure 16) and the filter support bars (Figure 17), were refined as the device was in its final stages of development. Several minor changes were made prior to fabrication, such as aspects of the washer and gasket design and placement and slight adjustments in dimensions. Critical interfaces received much attention in order to assure the best fits possible.

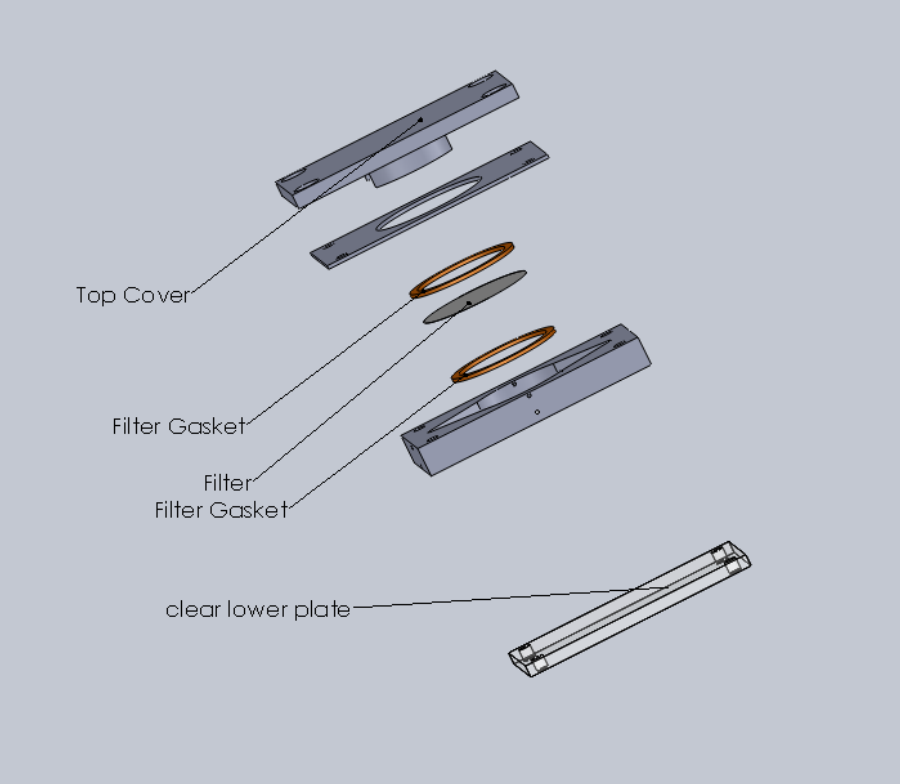

Figure 15 -- Design shown largely similar to final design.

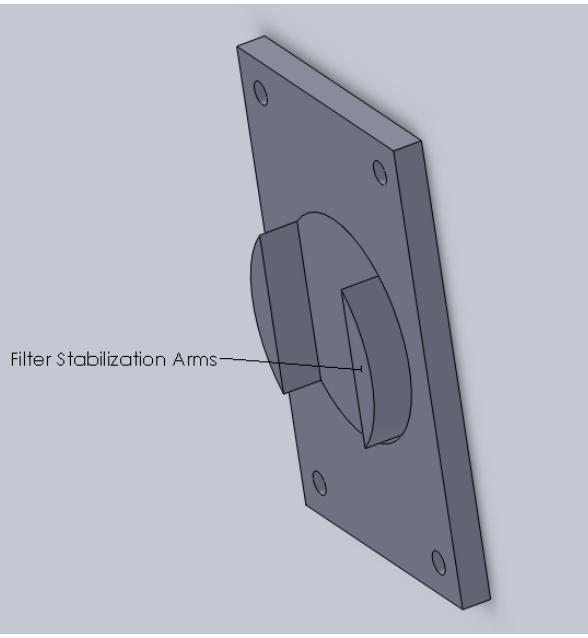

Figure 16 -- A critical aspect of the design development was the implementation of the filter stabilization arms, which are intended, in conjunction with rubber washers, to secure the filtration membrane in the device.

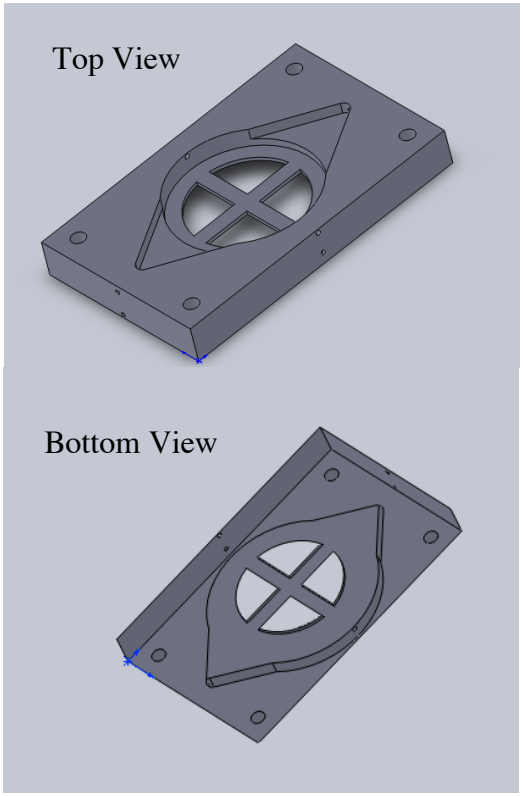

Figure 17 -- A second critical design modification -- the filter support bars, intended to keep membrane in place and level were added to the middle part.

Thus far in the device development, the large-scale geometries have become well established. However, many important details integral to the function of the device have not been addressed. For example, concrete designs for the fluidic ports and electrodes were not established until much later in the design development iterative cycle. For example, many of the previous models show two holes on each of the long sides of the middle acrylic parts, which were initially intended as electrode connection ports, perhaps via an alligator or banana clip, to the Labsmith™ High Voltage Sequencer (HVS). However, an exact plan for these connections was not developed until later, as many questions related to the electrode design remained unanswered at this point. To that effect, the electrodes have not been shown in any of the Solidworks™ renderings thus far.

The other critical areas with an unclear design were the fluidic ports. Initially, Luer-lock style connectors for the device ports were explored as a reliable and leak-proof fluidic connection that could withstand repeated assembly/disassembly cycles. Eventually, this design was replaced by a seemingly simpler method, wherein stainless steel syringe tubing was press-fit into ports on the device. Details and secondary modifications of this design will be described further, as will the final design prior to fabrication.

Final Design for Manufacturing

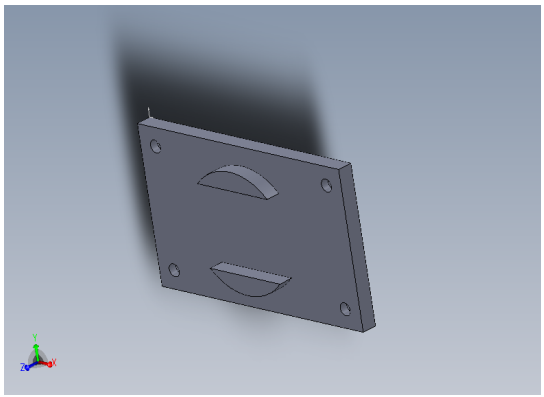

Figure 18 -- Solidworks® rendering of the version of the top part for CNC fabrication.

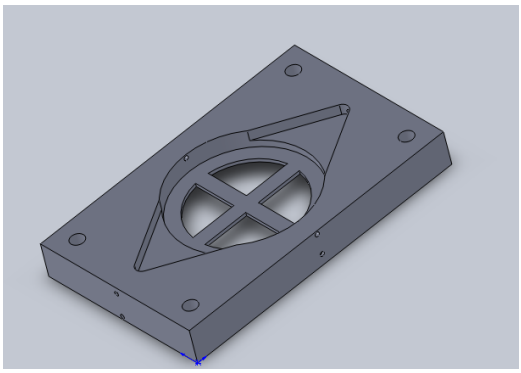

Figure 19 -- Solidworks® rendering of the version of the middle part for CNC fabrication.

This generation of the device was the final design prior to fabrication. The models Figure 18 and Figure 19 were used to program the CNC mill for the fabrication of the top of middle pieces.

3.2 Material Selection

We selected acrylic plastic as the most desirable material for the housing and structure of the device. Acrylic plastic has several qualities that contribute positively toward the goals of the device including optical clarity, ease of fabrication, strength, availability, and prior experience with its use personally and in other projects of our lab. This material makes up the bulk of material used in this device. Depending on the part geometries, the acrylic potentially could be milled, LASER cut, and manipulated with any other appropriate material removal tools. Also, acrylic parts can be fastened via chemical bonding, as well as traditional mechanical fasteners.

Through the design development, the necessity for gaskets, O-rings, and other sealing components became apparent. Because of the non-standard sizes and dimensions of the components, simply purchasing a correctly sized O-ring was not possible. While it is possible to order custom-sized gaskets, the cost of acquiring such parts is prohibitive. Consequently, bulk rubber gasket sheeting was selected for the design, as the complex geometries needed could be easily cut with the LASER cutter in the Mustang ’60 machine shop. The initial gasket material (McMaster-Carr #9470k27) did not cut easily with the laser cutter and is exceedingly stiff due to the incorporation of aramid fibers with a BUNA-N binder. After experimenting with this material and determining that the properties were not suitable both for fabrication with laser cutter and sealing properties in the device, a replacement gasket material was found at the local hardware store (Ace

Hardware). This material is much more pliable and compliant than the previous material. The following sections will describe how this material was cut and modified over the design and manufacturing iterations and the corresponding results. Cutting this material in the laser cutter was a success and future students should consider it for their own use in the fabrication of gaskets or other uses of the material in unique geometries.

The socket cap screws used in this experiment were chosen because of their wide range of sizes and ease of use. In order to perform the necessary experiments, the device needs to be taken apart and re-assembled with ease. Socket cap screws allow for easy assembly with an Allen wrench. Choosing stainless steel hardware has helped avoid problems with corrosion, especially considering the combined fluidic and electrical components of the device.

The tubing used in this device is Tygon™ clear laboratory tubing. As the final design was tested and re-iterated, some tubing dimensions were changed, but the overall type of tubing was unchanged. This tubing has been used in our lab for many projects and is preferred for its mechanical properties, small inner bore, biocompatible material properties, and optical clarity. Most of the tubing connections were made with the 23-gauge stainless steel syringe tubing. This product made tubing attachment and disconnection simple and did not require the use of epoxies or other adhesives to create a watertight connection. This technique helped to satisfy the goal of developing a device that could be easily and fully disassembled.

3.3 Major Fabrication

3.3.1 Gasket and Washer Fabrication

The following set of parameters in Table 1 is adapted from the ULS X2 660 manual for making rubber stamps. The laser cutter, seen in Figure 20, was set up in this fashion to cut the rubber gaskets. This trial was simply based on the assumption that the gasket material would behave similarly to the rubber stamp example in the manual, as the technicians in Mustang '60 are more accustomed to cutting thermoplastics, not rubber. The working height is another consideration that must be checked prior to operation. This ensures the distance from the tip of the laser to the part is correct. Some important safety considerations include ensuring the exhaust fan is on, as the process emits toxic gases, and working as well as avoiding looking directly at the laser when the machine is running to avoid eye damage.

Table 3 -- Shows the parameters used in the laser cutter to cut the rubber gasket material.

Parameter	Value
PPI	90
Wattage	30
Power	60%
Speed	1.60%
Expected Depth	0.040"

These parameters, with the exception of the "Expected Depth," are entered into the properties of the laser cutter printer set up. Because the "Expected Depth" is 0.040 inches and the material is 0.0625 inches thick, two passes are required to cut the material. AutoCAD™ , which is compatible with the laser cutter, was used to draw and dimension the part. The operation of the laser cutter is controlled through printer style dialogues, as the movement of the laser is constrained to two dimensions similar to a printer. Other

software, such as Adobe Illustrator™ can be used with this machine as well, but AutoCAD™ is better suited for technical engineering applications.

The laser cutter did not cut this gasket material cleanly. The cut edges were extremely rough and charred, and had be sanded or filed in order to smooth and remove the undesirable material. Also, after some initial assemblies, this material was deemed too stiff for this application and another material was located to properly gasket the device.

Figure 20 -- Image shows the ULS X2-660 laser cutter used to cut acrylic sheet and rubber gaskets. The material shown is 1/16" acrylic.

Because the first gasket material was not suitable for this application, we replaced the gasket material with one of lower durometer and different material properties. This material is also inexpensive and can be found at Ace Hardware. Because it is much more pliable, we hypothesized that it would seal the device more effectively. We used the same properties as above when cutting in laser cutter and the result is a very smooth, defect free cut surface. This material had no charred or irregular edges, but simply left

behind a fine dust. This material was much more desirable than the initial material and we highly recommend this method.

Over the course of the device fabrication, numerous gasket techniques and geometries were produced. These revisions were motivated by difficulties forming watertight seals in the device, as well as to accommodate other design changes in the acrylic housing. Having an inexpensive material that is easily manipulated with the laser cutter was helpful, as it allowed several design and fabrication iterations to be tested in a timely manner.

3.3.2 CNC Machining of Top and Middle Acrylic Parts

This section describes the fabrication of the top and middle parts, but a more detailed descriptions and instructions for CNC mill operation may be found in Appendix A. In order to prepare for the fabrication of filter housing, stock half-inch thick acrylic sheet was rough cut into the approximate size needed with a vertical band saw and then finished on the mill to 4 X 2.5 X 0.5 +/- 0.001 inches. The precision of this initial cutting operation was important, as these pieces were next machined with the CNC mill to their final specifications. Because the top and middle pieces were drilled for fasteners and other features that were required to mate precisely, careful dimensioning and machining was imperative. The following image, Figure 21, shows a progression of the top part fabrication in the CNC mill.

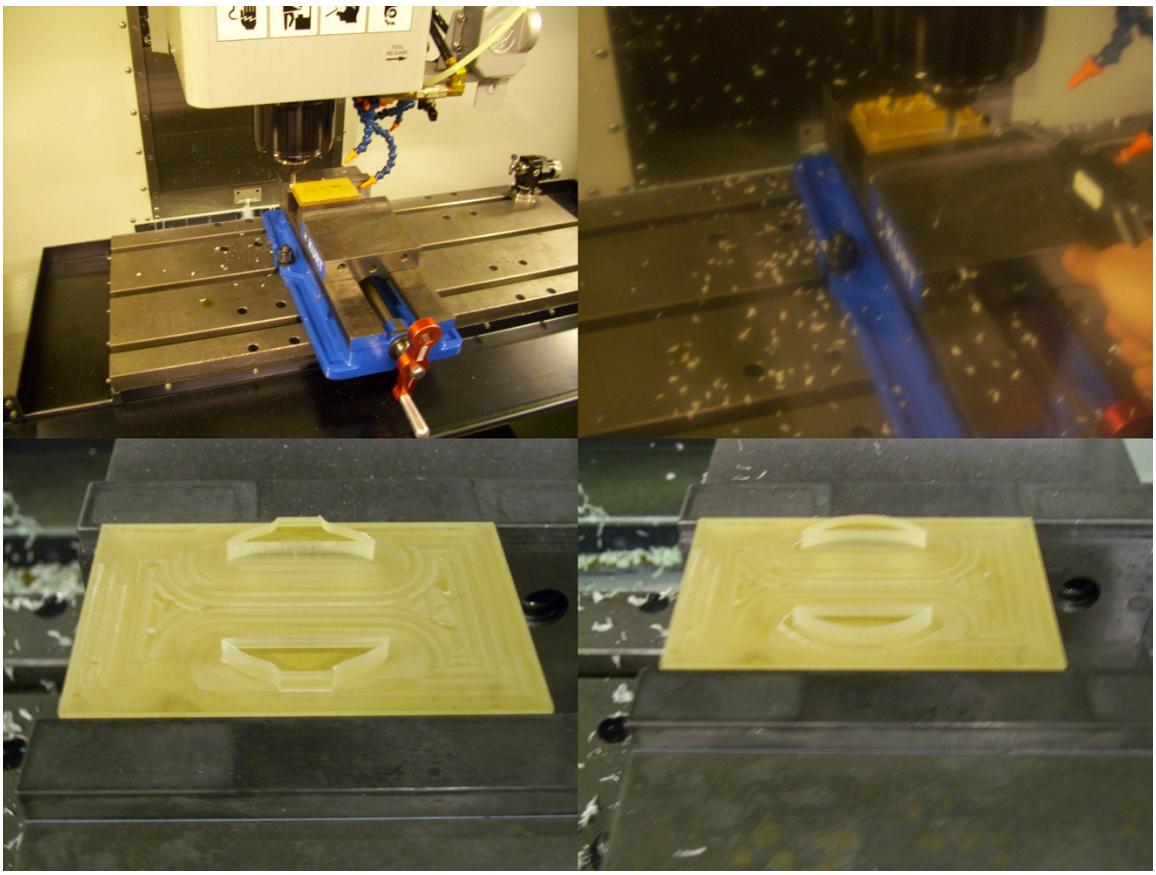

Figure 21 -- Fabrication of the top part, specifically the curved membrane stabilization arms. The lines across the face of the part were a result of an excessively high feed rate, but were easily sanded out.

The essential features of the top and middle parts, as seen in Figure 21 and Figure 22, were fabricated with the CNC mill. For the CNC mill operations, several procedures prior to actual fabrication processes took place. First, the CAD model was submitted to the machinist (Robby Nielson) and the Mastercam® file was developed. This program acts as a bridge between the CAD model and the computer in the CNC mill, as it outputs instructions in the language that the CNC mill can interpret. Included in these instructions are tool paths, tool selections, spindle speeds, and feed rates. For example, different end mills and feed rates were used for the rough cuts as opposed to the finishing cuts of the filter stabilization arms, as seen in the bottom left and right images in Figure

21, respectively. Prior to machining, all of the parameters, both in the Mastercam® software and the settings on the CNC mill must be double-checked. Errors are a serious risk to the part being fabricated as well as the machine and the operator, as miscalculations can easily cause the machine to crash. For this reason, we performed "dry" runs prior to the actual machining operation by running the machine with the table lowered. In this fashion, one can watch the function of the machine without actually cutting any material, as the endmill stays several inches above the part. Key observations during the test run include tool changes, spindle speeds, and feed rates. For example, we found a problem with the origin of the part, meaning the part was not in the location the machine was told. If the dry run had not been performed, the machine could have crashed into the parallels or into the vise.

During the CNC mill fabrication process, some adjustments were made to the parameters used. For example, the top part was machined first with a feed rate of sixteen feet per minute. This feed rate was too fast and left visible lines (clearly seen in Figure 21) between each pass, as material was not removed as smoothly and cleanly as it should. After noting these imperfections, the feed rate was reduced to eight feet per minute for most other operations. We reduced the feed rate further when the material for the pocket openings of the middle part (bottom left of Figure 22) was removed, in order to reduce the chance of a fracture. Because of the ease of machining acrylic, all operations were performed at full depth, except for the finishing pass. At the 8 feet per minute feed rate, this finishing pass resulted in excellent surface finishes and precisely aligned features. In addition, we used an air gun to keep the flutes of the endmill clear of chips and debris that could have otherwise reduced the quality of the cuts. Chip removal is often

important when working with acrylic and other thermoplastics, as the debris has a tendency to heat up and melt back into the part. Similarly, these materials can be sensitive to excessive feed rates and spindle speeds and chips will melt instead of being cleanly removed from the part.

For both parts, after the endmill operations, we programmed the CNC to drill the holes for #10-32 bolts. Holes in the top part were drilled for #10-32 clearance with a #10 bit, while the holes for the middle part were drilled with a #21 bit for the tapping of their internal threads. These holes were tapped later by hand, in conjunction with other supplementary operations. At completion of the CNC milling, the parts were cleaned, photographed, and measured in order to verify correct geometries and dimensions. The following image, Figure 22, shows some of the CNC fabrication of the middle part.

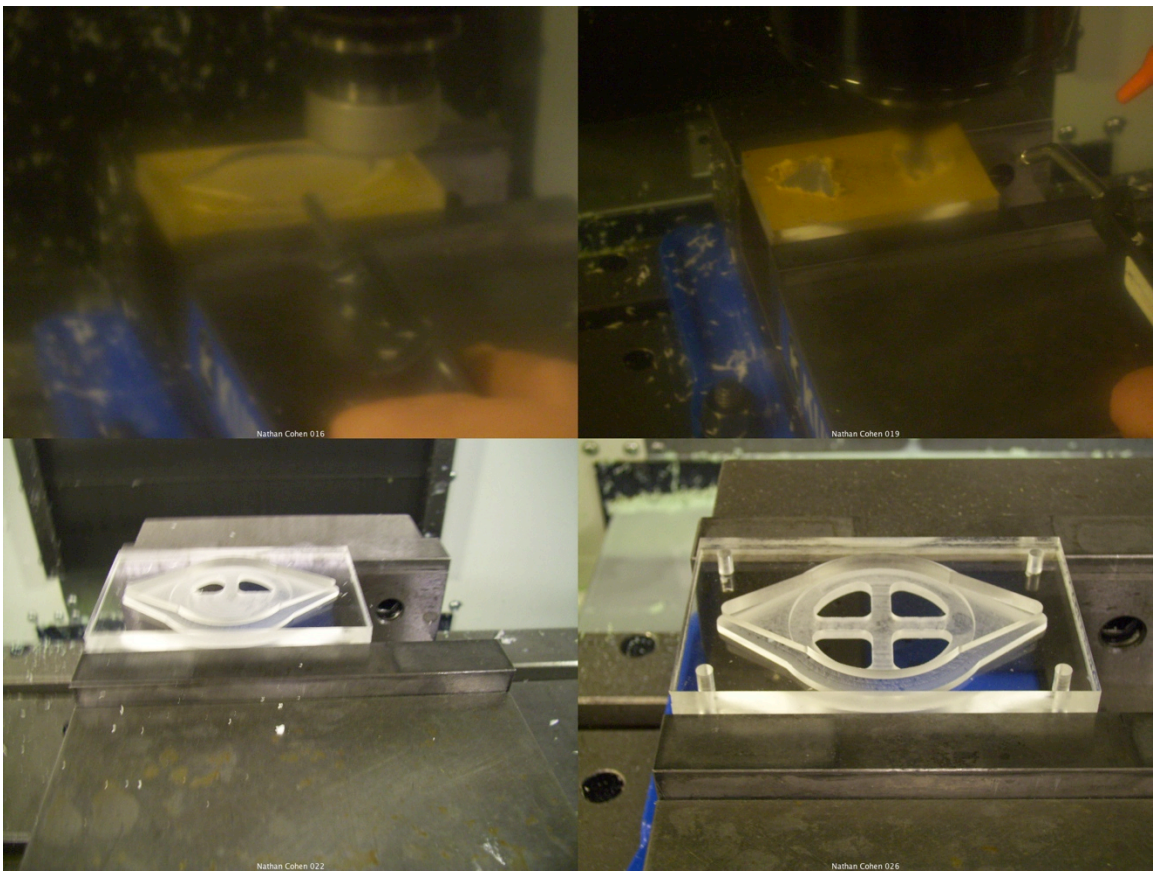

Figure 22 – Image shows a montage of the CNC milling of the middle part.

In addition to the CNC mill, various aspects of the design other than the gaskets were fabricated with the ULS X2-660 laser cutter. The laser cutter can be used effectively to cut thin acrylic and other thermoplastics. Initially, the bottom cover of the device was cut from 1/16-inch acrylic sheet with the laser cutter, which again allowed for parts to be prototyped in a time efficient manner. If many of these other parts had to be machined multiple times on the mill or CNC mill, the prototyping time would have been much longer.

4 Further Fabrication and Part Development

The inlet and outlet ports were not fabricated until after the CNC milling phase was finished. The simplest, most reliable design was selected. This design applied a simple interference fit between the filter housing and the stainless steel syringe tubing, wherein the stainless steel tubing is pressed into the housing and Tygon™ tubing fastened directly with no adhesives necessary.

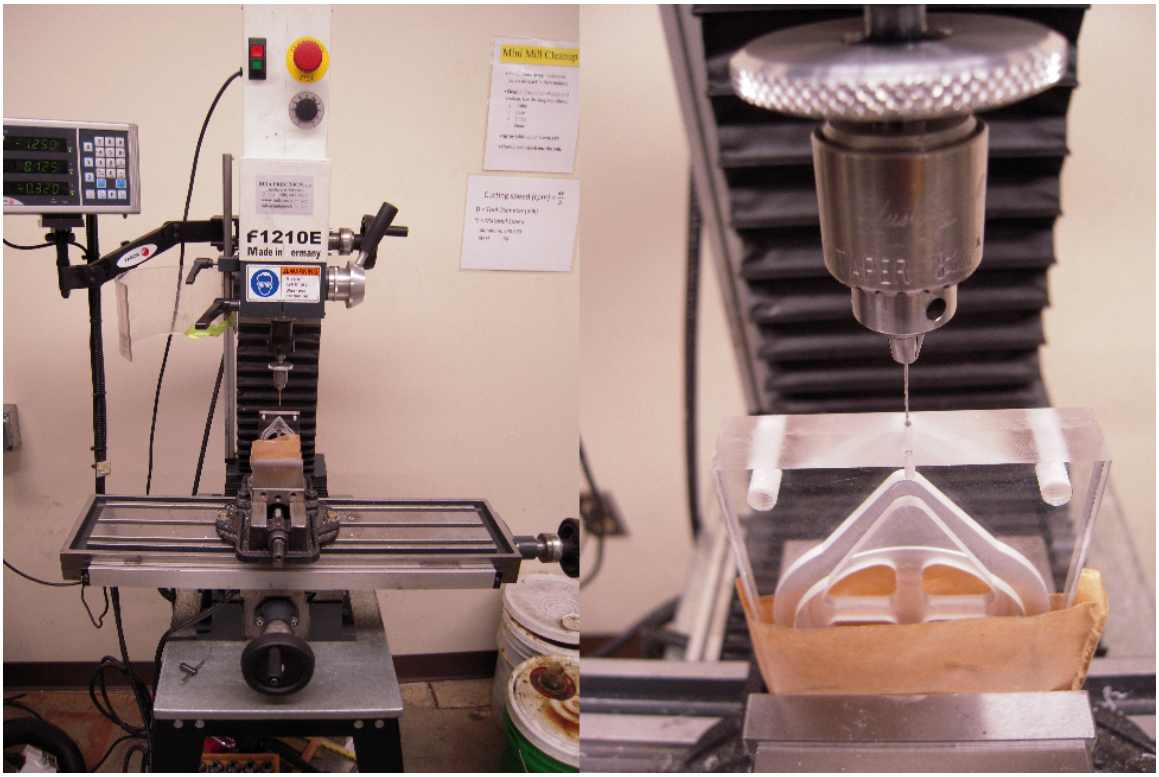

Figure 23 -- Holes for fluidic ports were drilled on the Mini-Mill™ in the Mustang '60 machine shop in the Bonderson building.

To further refine this design, we drilled 1/16 inch diameter blind holes into the housing to a depth of approximately 0.15 inches. This allowed the Tygon® tubing to be seated against the device. Then, the through holes for the stainless steel syringe tubing were drilled with the #74 (diameter = 0.0225 inches) drill bit. Because this bit is so small and fragile, a special drill chuck made for small diameter bits was required. This chuck,

a type of pin chuck, must be carefully extended by hand to drill the hole. Of course, because of the extremely small diameter, the spindle speed must be much higher than that of the average diameter drill bit and endmill.

4.1.1 **Electrodes**

We fabricated the electrodes from forty gauge copper wire (extremely fine wire). This thin wire allowed for easy manipulation and fit into the assembly of the filtration housing. The bottom electrode was simply adhered to the underside of the middle part along the circular bottom chamber and attached to conductive tape. This tape fit between the middle part and the bottom washer and extended out of the device just long enough for an alligator clip to be used to make the electrical connection.

Similar to the bottom electrode, the top electrode was adhered to the circular washer, which fit in between the top part and the filtration membrane. This electrode also used conductive tape to form a tab for connecting an alligator clip. This electrode method was a critical means of fulfilling our goals for inexpensive and straightforward fabrication procedures.

Because of the incredibly small diameter of the electrode wire, power considerations must be made. Any wire will have limitations on the amount of amperage it can handle without excessive heating and damage, and wire this small in diameter has an incredibly small tolerance for high currents. Eq. (9) shows a calculation for the maximum amperage versus the diameter of a wire—the point that generates temperatures high enough for melting. Obviously, the operation is desirable only well below this limit.

$$I = kd^{3/2} \quad \textbf{(9)}$$

where,

I = electrical current (Amps)

k = fusing constant

d = wire diameter

The constant in the above equation is known as the fusing constant. For our copper wire, this equation yields a maximum current of 1.8 amps. The expected values are on the order of micro-amps, so actual amperage should be several orders of magnitude below the maximum.

4.1.2 **Stainless Steel Tubing**

Because the stainless steel syringe tubing was purchased in long lengths, it must be cut to length prior to use. Wire cutters generally crimp the ends of the tubing, which does not allow proper flow through the lumen of the tubing. Alternatively, one can use a sharp razor blade to cut the tubing. When using a sharp razor blade, one can apply steady pressure to the tubing against a hard surface, such as a countertop, and the tubing rolled carefully back and forth until the piece separates. This technique is effective but time consuming, not particularly easy, and consumes several razor blades. A different method that is just as effective just requires the cut end of the tubing to be filed after cutting with decent wire cutters. Filing the end can remove any material that got folded inward when cut with the wire cutters, so that the end of the tubing is left free of obstructions. One

should ensure the cut end of the tubing is not excessively sharp or have any burrs, as this can damage the Tygon™ tubing and lead to poor connections.

4.1.3 **Logistical Issues for Imaging and Validation**

We addressed challenges related to the final operation and validation of the device in parallel to the fabrication steps and design iterations. Often, trial fabrications or subsequent assemblies of parts would confirm that design or validation techniques were not viable. Because of these trials, we were able to adjust and streamline parts until they proved adequate. The fluidic leakage issues and changes for validation purposes generated the most changes and adjustments during the fabrication process.

Early in the design phase, the Labsmith™ inverted video microscopes were intended as the major tool for validation. This concept was integral to the initial design, as decent visualization requires optical clarity and the target plane must be within the maximum focal length of the microscope, not to mention several other logistical parameters. After the first assemblies, wherein the device leaked significantly, which is highly undesirable when placed upon a microscope, changes were required. Using a stiffer bottom cover piece ameliorated leakage taking place between the bottom of the middle part and the bottom cover. Specifically, the original design called for the bottom piece to be made from 1/16-inch thick acrylic in conjunction with a rubber gasket. However, with bolts providing compressive force only at each corner of the device housing, the middle of the mating surfaces did not experience enough compression to seal effectively. In fact, this thin acrylic sheet bends out of plane when the bolts are tightened, causing a visible gap between the materials in the center of the device.

Researching the proper use of gaskets and mechanical sealing revealed this leakage as a nontrivial, but common, problem. Several equations and approximations exist to estimate the sealing forces needed between two coupled parts to seal against certain ranges of internal fluid pressures. Perhaps the most influential of these variables is the number of fasteners per length of mating surfaces. However, because of the geometric constraints of the device thus far, the addition of more fasteners seemed impractical. So, in order to seal the bottom of the device without the addition of fasteners, a stiffer bottom cover, which would more evenly distribute the compressive forces from the corner bolts, replaced the original bottom cover. For this part, we used the same half-inch thick acrylic stock, same stock as that used for the top and middle parts. To assemble this piece, we match drilled each corner clearance holes and bolted it to rest of the device using #10-32 bolts threaded into the base of the middle part.

This method effectively seals the base of the unit, but adds an extra 0.5 inches of thickness to the device, which causes an equivalent increase in the required focal distance needed for visualization through the base. However, at this point in the development, visualization with the inverted microscope appeared inappropriate and likely impossible. For this reason, other options for validation were explored and the fabrication and assembly processes were continued in new directions.

The other possible visualization technique was to utilize Professor Lily Laiho's upright Olympus™ BX-41 fluorescent microscope. In general, this technique is more appropriate than using the inverted microscope, as the filtration membrane and processes should be visualized from the top down. In addition, the 10X objective on this microscope has a relatively large maximum focal distance of about eight millimeters.

While particle visualization may still not be straightforward, this route offered a much more realistic approach than the inverted microscope. We consulted Dr. Laiho and discussed some logistical requirements, such as the ability to operate the device without leakage. Essentially, if the filtration membrane could be visualized while the device operates, a quantitative and qualitative assessment of particles depositions onto the membrane as well as paths of travel over and/or through the pores could be assessed. However, with the particles traveling in the vertical direction, any particle movement away from the membrane would be out of the plane in focus. Nonetheless, counting particle movement into or out of the focal plane could provide sufficient information to determine any difference when the electric field is active.

While the focal length of the 10X objective in the upright microscope is rather large, it still is not long enough to accommodate the thickness of the top cover. Hence, the top cover needed to be modified to reduce the thickness and allow for imaging. This reduction was accomplished by milling out a rectangle in the center of the top part and inserting a 1/16-inch recessed Plexiglass™ "window." This window was inset in the top of the middle part, such that it was held between the top part and the middle part. The modification of the middle part can be seen in Figure 24. Unfortunately, the extra mating surfaces were another source of leakage. Often, after the device was modified, we ran water tightness tests, which simply consisted of pumping fluid through the device at flow rates in the same range as the experimental flow rates.

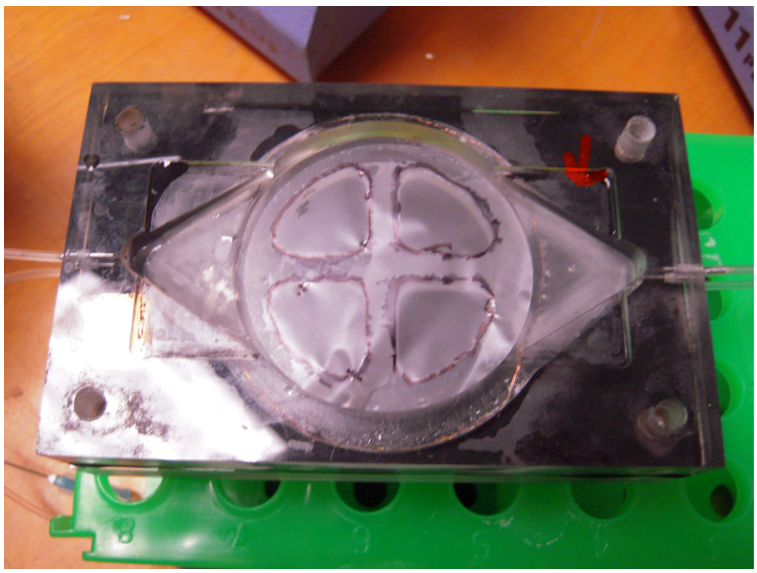

Figure 24 -- Shows the recessed area, an example indicated by the red arrow, of the middle part milled out for the "window" part.

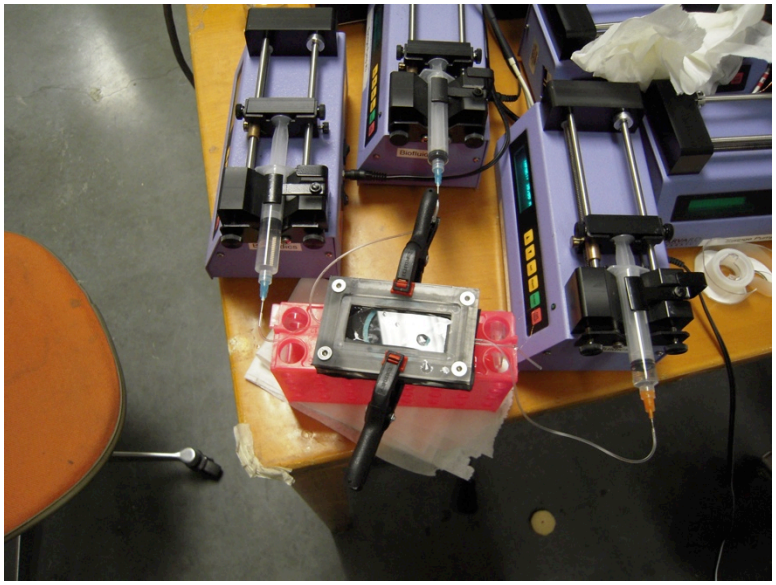

Figure 25 -- Shows the experimental setup as watertightness was evaluated. In this particular example, clamps were used to help compress the midpoint of the device together in attempt to form an adequate seal.

The clamps in the figure were ineffective for sealing the unit, but the idea of applying compressive force more evenly to the device continued to be explored.

The following image, Figure 26, shows one example of fluid leakage out of the device. In this case, fluid is leaking from the junction of the top part [gasket] and the

window area. Unfortunately, this area was the most problematic source of leakage and as the device iterations were tested, there was an obvious need to fix this issue.

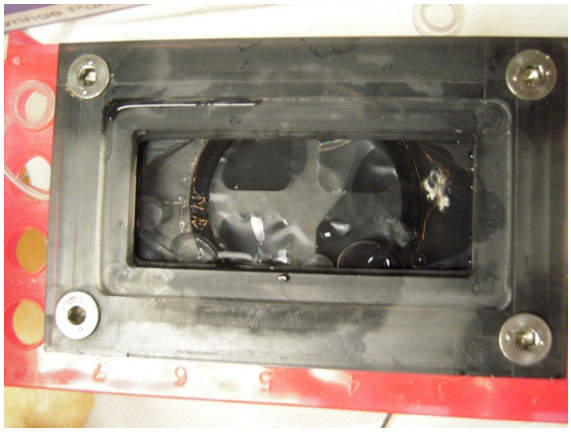

Figure 26 -- Prior to final leak proofing, fluid was seen leaking between the interface of the top part and the viewing window.

4.1.4 Use bolts around the perimeter

In the final attempt to solve the leakage issues, we used eight additional bolts around the perimeter of the device to maintain a more even pressure around the edges of the device. We drilled clearance holes through top and middle parts and used 1-1/4 inch long bolts to clamp all three major parts of the device together. The base was tapped for #4-40, such that the bolts applied pressure both to the top/middle gasket as well as the middle/bottom gasket. The bolts are spaced roughly one-inch apart, apply a much more consistent clamping force on the perimeter of the device. The following image shows the device with the addition of these bolts.

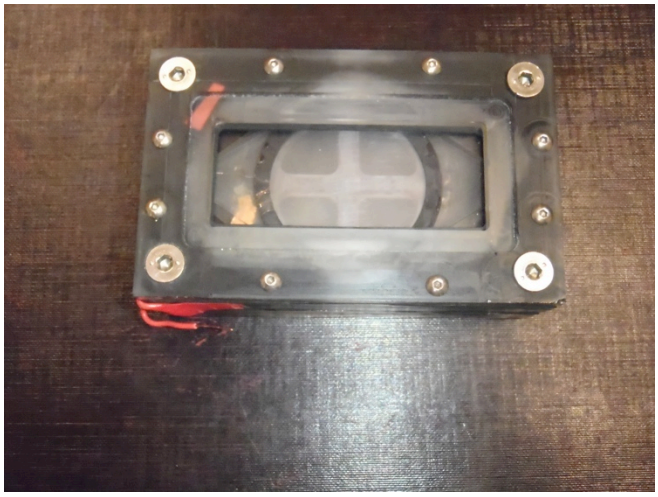

Figure 27 -- This image shows the device with the addition of the #4-40 perimeter bolts, which were critical for leak proofing.

The extra bolts sealed the device around the outside perimeter of the housing, which was an important step in the device sealing process. In fact, the device remained sealed around the perimeter even when the original corner bolts were loosely secured.

4.1.5 Flow and Pressure Limitations

Initially, the tubing and connections used in the device were the same as those used in the microfluidics work in our lab. This design was selected in part to make this

device interface with the other equipment in the lab. However, because this device requires a substantially higher flow than most other devices in the lab, whether or not the small diameter Tygon® tubing would allow for enough flow volume was a concern. So, initially, tubing having an internal diameter of only 0.020" was used. In order to verify that this tubing would provide enough flow volume, the Hagen-Poisseuile equation was used to estimate the maximum flow the syringe pumps could sustain with such as small diameter tubing. With the 60 mL syringes, the pumps are capable of producing a maximum of 8 PSI. Using this maximum pressure, tubing radius and length, the calculated maximum volumetric flow rate is roughly 54 mL/min. In theory, this flow rate should be sufficient for the proper operation of the device.

However, this calculation did not take into account the smaller inner diameter of the stainless steel syringe tubing that was used in the fluid connections. Initial testing showed the resistance in the tubing and connections was too great and the flow not sufficient. Consequently, the tubing was changed to a different Tygon™ product (Small Parts # NE-161PL-25) with an inner diameter of 1/16", three times the inner diameter of the original tubing. Because the radius term in the flow equation is raised to the fourth power, this increase in diameter corresponds to an immense increase in flow rate and corresponding decrease in the required pressure.

To accommodate for the larger tubing, new Luer-Lock syringe tips (Small Parts # NE-161PL-25) had to be obtained. Also, the fluid ports had to be expanded to fit the new tubing and connectors. The though hole for the stainless steel connectors were enlarged to 1/16" and the larger blind port segment was enlarged to 1/8" to fit the outer diameter of the new tubing.

4.1.6 Seal window with RTV

With the added bolts around the perimeter of the device, the gasket is clearly more evenly compressed around the entire perimeter. However, at this point, the junction of the thin acrylic viewing window leaks. During this water-tightness test, the smaller Tygon™ tubing was still in use. After the device was modified for the larger tubing diameter, it was tested again for leaks. The device still leaked at the window junction, so we decided that we needed an adhesive or sealant to rid the device of the leak. Adding more mechanical fasteners to the device was impractical because of the geometric constraints and associated increase in assembly/disassembly effort. So, to fix this last point of leakage, silicone Room Temperature Vulcanizing (RTV) sealant was applied to this junction. This sealant still allowed the top assembly (top acrylic piece, top gasket, and acrylic window piece to be removed so that the filtration membrane can be exchanged. However, the individual top pieces remain adhered to one another unless the RTV is removed. Unfortunately, visualization into the device through the "window" was slightly impaired after the addition of the clear RTV, which made device operation slightly less convenient, but was not a serious issue functionally.

4.2 Preliminary Testing

4.2.1 Electrolysis

Oftentimes, fluidic devices having exposed electrodes in conductive fluids have issues with electrolysis, which causes gaseous bubbles, often complicating sensitive flow environments, altering electrical properties of the fluid, or causing imaging complications. Some images were taken with the electrodes active (ramping voltage up

from zero to twenty volts). At no time was bubble formation visible, perhaps because of the low conductivity of the fluid and low amperage of the DC electrode configuration.

4.2.2 Fluid visualization with food dye

Several attempts were made to visually confirm an appropriate flow profile through the device. Early in the preliminary testing, these efforts were confounded by issues with fluid and leakage and large air pockets. However, after the leakage issues were abated and priming methods that removed the air pockets were developed, a uniform flow profile was seen in the device, as seen in Figure 28. In addition to a smooth flow profile, the green food coloring used for visualization began to color both the filtrate and retentate solutions, which suggested the fluid flow was behaving in a similar fashion as intended. An example of the fluid flow not behaving as expected may be if no green food coloring were to appear in the retentate.

Figure 28 -- Image of basic fluid flow verification, performed by introducing a bolus of green fluid (dyed with food coloring) via the suspension inlet port. Device was primed with buffer and operated at 8 mL/min influx and 2 mL/min outlet volumetric flow rates, respectively.

Furthermore, the following image, Figure 29, was taken to capture the way in which the device is cleared of suspension and fluid. The validation techniques used required that the chamber be cleared of fluid before analysis. This clearing was essential because any leftover fluid in the device could potentially disturb or flush away particles seated on the filtration membrane. However, the development of this technique required, in the very least, visualization of the fluid flow as it is drawn out of the device. This final step in the experimental process is critical, but was difficult to predict how exactly the fluid behaves as air is allowed into the device. Generally, the fluid fraction remained intact as it was extracted from the device, meaning that air replaced solution consistently from left to right. Once the outflow syringes began to draw in air bubbles, the device had cleared of solution and was ready for disassembly and analysis. If present, excessive mixing and vorticity may have suggested significant disruptions of the particles on the membrane, likely causing unpredictable variations in the data. As few reasonable ways existed to clear the chamber and prepare for analysis, this method seemed most appropriate and repeatable enough for fair comparisons among experiments.

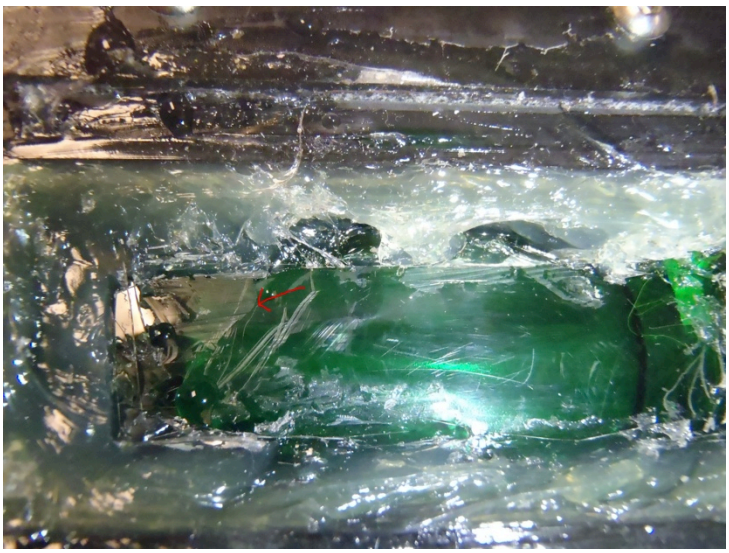

Figure 29 -- Image of flow during "clearing" phase of device testing operation using green food coloring. Standard procedures were used, such that influx syringes were disconnected and arrested, while syringes in vacuum cleared device of fluid.

The green fluid in the picture above shows how the fluid behaves when suctioned out of the device. The red arrow shows the “trailing edge” of the fluid that is being removed from the device.

4.3 Validation

Several methods of validation were explored in order to quantify the function of the device. Some methods focused on the analysis of the filtration membrane while others quantified the composition of the retentate solution. Ideally, both of these aspects could be verified using available resources here at Cal Poly. Unfortunately, filtration membrane analysis was found to be the only viable validation technique. The following section describes proposed validation techniques, concluding with the technique found most appropriate and subsequently performed.

4.3.1 Viscometry

The Vilastic Vmax™ viscometer was explored as a means of quantifying the number of particles in the retentate solution. The number of particles in a solvent solution can be back-calculated from Einstein's Equation for Viscosity (Eq. (10)),

$$\mu = \mu_0(1 + 2.5\phi) \quad \textbf{(10)}$$

μ = viscosity of solution

μ_0 = viscosity of solvent

ϕ = volume fraction of particles

This equation stipulates a low volume fraction of particles, such that there is no particle-particle interaction. Because the concentrations used in the experiments were extremely small, this assumption is not violated. The equation is accurate for a very wide range of particle diameters (from molecular models as spheres to spheres of hundreds of microns), the particles used in this experimentation certainly lay within this range [28]. The plot below shows an experimental verification of Einstein's equation over the range of volume fractions where it applies linearly.

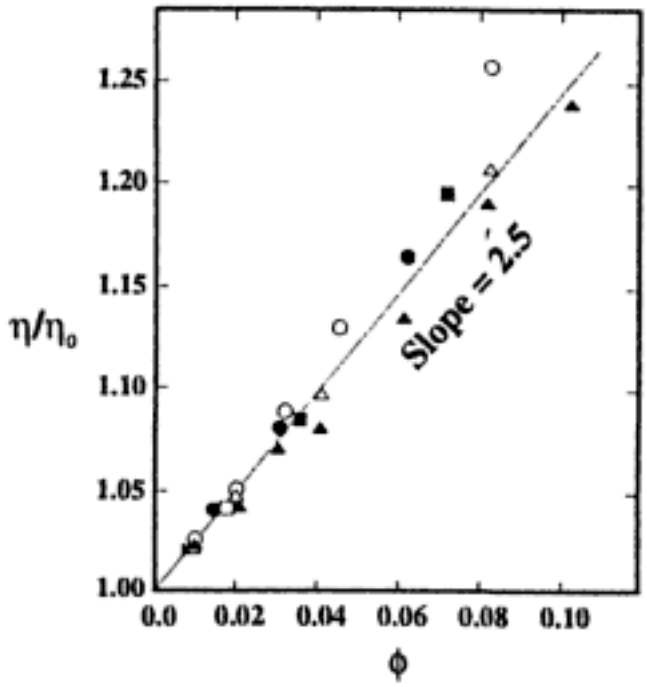

Figure 30 -- Shows viscosity data plotted against the volume fraction of particles in agreement with Einstein's Equation for viscosity.

Before experimental data was analyzed in this method, tests using known concentrations of beads were analyzed with the viscometer to confirm that it was possible to detect within the range of sample concentrations expected in our retentate. For this test, the viscosities of de-ionized water, buffer solution, a 6μm bead solution, and a 10μm bead solution were measured as summarized in the table below.

Table 4 -- Average Viscosities of Known Concentrations of Solutions

Viscosity Measurements				
Settings for "Stretch" protocol				
Frequency:	2			
Integration:	5 seconds			
Low Drive:	2			
High Drive:	5			
			Average Viscosity (Poise)	
Sample	Concentration	Volume Fraction (Φ)	Low Drive	High Drive
DI H2O	N/A	N/A	9.21E-03	9.27E-03
buffer	N/A	N/A	9.34E-03	9.30E-03
beads, 6 µm	42,000 beads/mL	4.75E-06	9.73E-03	9.69E-03
beads, 10µm	36,000 beads/mL	1.89E-05	9.54E-03	9.46E-03

After using the average viscosity values to calculate the volume fraction, the subsequent number of particles can be calculated using the volume of the individual spheres of known radius according to the following expressions, Eqs. (11) and (12).

$$\phi = \frac{NV_{particle}}{V_{total}} \tag{11}$$

$$N = \frac{\phi V_{total}}{V_{particle}} = \frac{\phi V_{total}}{\frac{4}{3}\pi R^3} \tag{12}$$

After performing these calculations, the volume fraction and concentration results from the viscosity measurement can be checked against the known values. Unfortunately, this technique was not sensitive enough to adequately differentiate between the different sample solutions, having far too much error. The incredibly small concentrations of

particles used in these experiments is likely much smaller than what is needed to detect any appreciable change in viscosity.

4.3.2 Conductivity

A similar idea to the viscometry approach was conceived pertaining to the conductivity of the solution, similar to the way in which a Coulter Counter operates, using conductivity, or conversely, impedance. However, there is little information in the literature about the way in which hard spheres in low concentrations affect conductivity. Kim and Torquato [29] have shown an increase in small, insulating hard spheres is correlated with a linear decrease in conductivity, but again, the concentrations and volume fractions of the samples used in the study were much higher than those in these filtration experiments.

We measured the conductivity of a number of particle solutions with known concentrations. The hypothesis of this was that, even at the small concentrations, there might be a detectable decrease in conductivity versus an increase in concentration of insulating particles in solution. Initially, as seen in the following graph, Figure 31, the expected correlation was found. The magnitude of the slope in this test is incredibly small (4E-5 μS/cm per particle/mL) but statistical analysis showed it significantly different from zero at the $\alpha = 0.05$ significance level.

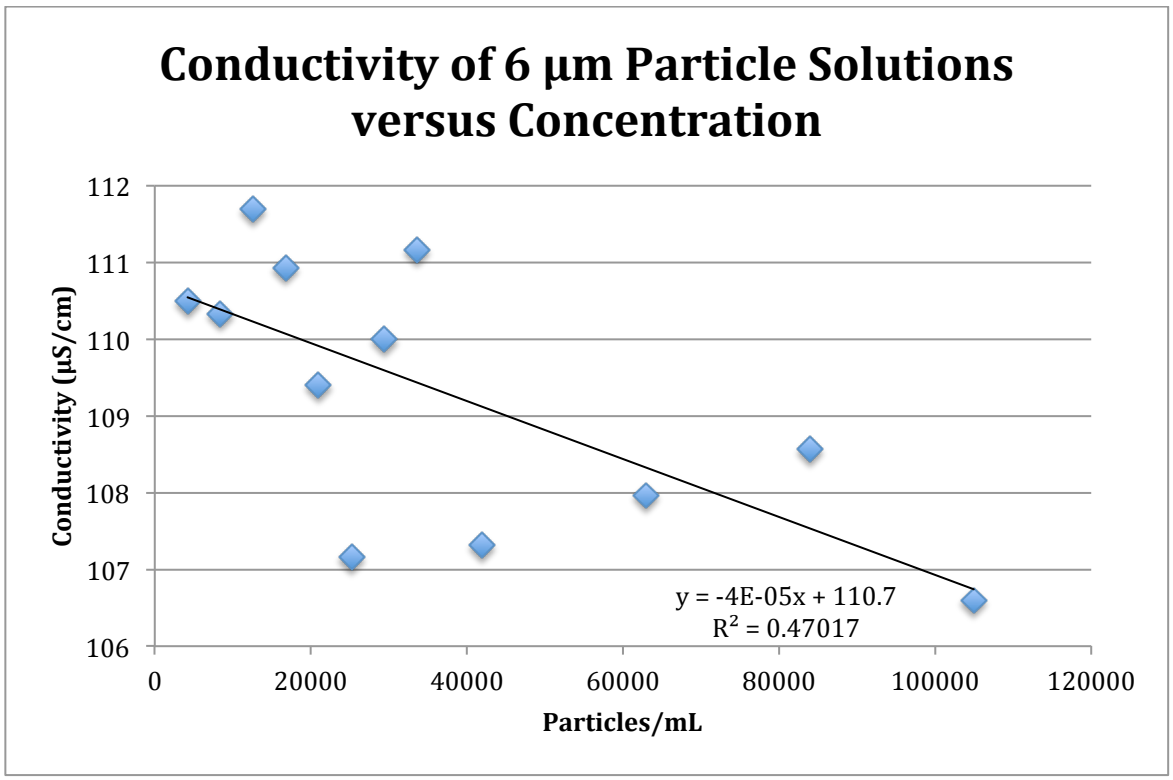

Figure 31 -- Expected correlation of particle concentration and conductivity with 6 μm polystyrene particles.

The results above shown in Figure 31 above supported the hypothesis and the value of the slope was within reason. However, subsequent tests resulted in data showing no trend or even opposing associations (positive slope). Therefore, the contradictory results simply demonstrated that the conductivity method was not sensitive enough for the small concentrations of beads. At concentrations as low as these, more sophisticated methods such as flow cytometry are necessary for particle quantification.

4.3.3 Microscopy Technique

Earlier, some difficulties associated with validation using microscopy while the device was in operation were mentioned. Due to the geometry of the device as well as many other logistical issues, *in situ* validation was not possible. However, similar to the conductivity and viscometry techniques, analysis can be performed after each filtration operation. We hypothesized that the filtration membranes could be imaged and the

number of particles deposited on the membrane could be counted after each test. For this method to work, the membranes would have to be removed from the filtration chamber and placed on glass slides to be imaged. This method depends on a successful transfer of the membrane from the device onto a slide. Initial trials showed that the particles and membranes were not affected by this handling step, as long as it was performed carefully using forceps on the very edge of the membrane, where there were no particles and flow. Once placed on the slide, the membrane can be easily imaged and the fluorescent particles counted. As this method was selected as the most appropriate and feasible means for this experiment, details of the experimental set-up and analysis follow.

4.3.4 Final Experiments

As explained above, it is hypothesized that, fewer particles will be deposited against the filtration membrane when the electric field is active than when off. This hypothesis is described below. (Note: The statistical convention of μ in the hypothesis statement is not related to the fluid, viscosity, electromagnetic, or other usages of the symbol found in this document.)

H_0: $\mu_{DEP} = \mu_{control}$

H_A: $\mu_{DEP} < \mu_{control}$

$\mu_{control}$ = the average number of particles per filter when no field is present

μ_{DEP} = the average number of particles per filter when DEP field is present

Some initial experiments of this type were performed in late Spring 2011. Expected results were not found from these initial tests, but much insight was gained from the early trials and tests. This helped improve the quality of the experiment and likely contributed to the quality of the end results.

The experimental set-up required four syringe pumps and the Labsmith® High Voltage Sequencer (HVS) and software. Four syringe pumps were needed, as one propels suspension into the upper chamber and one propels buffer into the lower fluidic chamber, and one pulls retentate from the top outflow port and one pulls permeate out of the bottom outflow port. Values predicted computationally and with the COMSOL™ models were used for the flow rates and electrode voltages. The following table shows a sample set of flow parameters that happen to be the most successful of various trials.

Table 5 – A typical set of flow parameters.

Flow Parameters	
Top Inflow (suspension)	8 mL/min
Bottom Inflow (buffer)	2 mL/min
Top Outflow (retentate)	2 mL/min
Bottom Outflow (permeate)	8 mL/min

Note that conservation of mass exists within the control volume of the chamber, as dm/dt (inflow) = dm/dt (outflow). So, as the system operates, there should be no change in the overall mass equilibrium and consistent pressure within the device. However, since the larger flow rate into the device is on top and the correspondingly large outflow rate (in vacuum) was configured for the permeate lower port, the majority of the fluid must flow through the filtration membrane. While this flow path can be deduced through conservation of mass and intuition, it was also confirmed with the COMSOL™ model in Figure 10. Using the values in Table 5, we know that there has to be roughly 6 mL/min of fluid flow through the filtration membrane. This value is referred to as Q_{filter}, and its expression is shown below in Eq. (13).

$$Q_{\text{filter}} = Q_{suspension\ inflow} - Q_{retentate\ outflow} \quad \textbf{(13)}$$

Figure 32 shows a sketch of the critical features of the device, including all four ports and their respective functions. As described above, the majority of the flow should travel from the suspension inlet through the filtration membrane and exit out of the outflow port. The buffer is necessary to maintain the conservation of mass in the whole system, as it balances out the outflow through the retentate port. The retentate port allows for particles levitated off the membrane surface to be collected in a separate vessel. However, because this system utilizes cross-flow filtration techniques, it would have less fouling than a traditional dead end filter, even with no active DEP force.

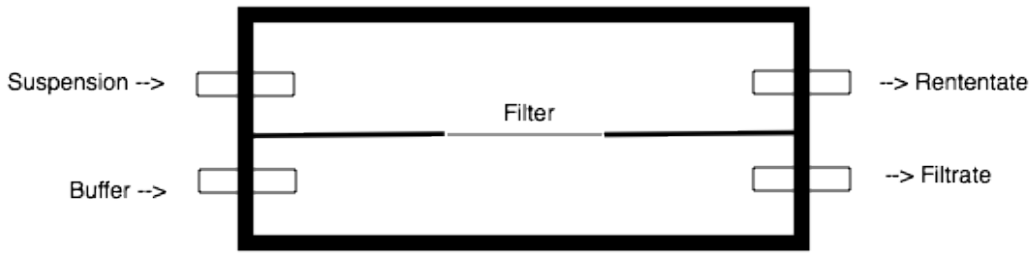

Figure 32 -- Sketch of filtration chambers and flow ports.

Prior to a test, the device must be assembled with the appropriate filtration membrane installed. For these experiments, either the six micron or eight micron pore diameter filters were used. The Millipore® membranes come stacked in their packaging, with paper discs of the same diameter separating one from the next. To protect from damaging the membranes, each was removed from the packaging with its paper "separator" on top. To place in the device, both the paper and the membrane were gently

laid into the filtration recess in the middle part with the tweezers. Most times, the membrane was laid smoothly--flat and evenly against the device support arms--and then the paper separator was removed. As they are extremely thin, considerable practice and care went into consistently placing the membranes smoothly.

Once the membrane was placed in the device, a permanent marker was used to delineate the edges of the filter support arms, such that the areas of the membrane actually available for flow were outlined. This step was important because these areas are the only place where it is appropriate to analyze the particles on the membrane, as there is no flow through other areas, such as the filter support areas and the gasket around the perimeter. The following figure, Figure 33, shows the membrane after being placed atop the middle part of the device. The block dots along the edge of the filter support bars show the border of the area where flow will occur.

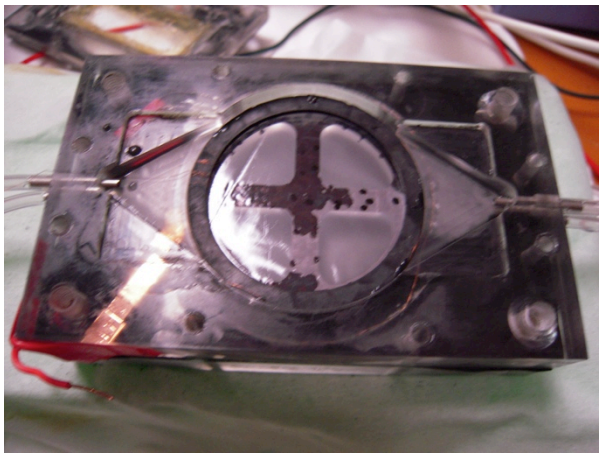

Figure 33 -- The filtration membrane, having its flow areas marked, and the washer placement over it.

Filling the device with buffer fluid prior to operation was critical to a successful operation. To fill the device, we loaded the inflow syringes with buffer solution and connected it to the device. The outflow lines were left unconnected. After turning the inflow syringes, the device was held vertically, with the outflow lines at the top, such that

all the air in the device could escape as it filled with fluid. This filling technique was one of the advancements resulting from the initial experimentation during the spring of 2011. While simple, this method eliminated large air pockets that would otherwise disturb the flow and electric field. During that initial testing, we observed many air pockets, which likely confounded the results of that round of testing. Unfortunately, at that time, this method of filling and air removal had not been utilized. Also, at that time, the device had issues with leakage, which may have not only resulted in solution leaking out of the device, but also air leaking into the device.

The buffer solution used in these tests was composed simply of deionized water and sodium chloride. Per the research of Kang et al., as mentioned prior, a target conductivity of 100 μS/cm was desired. This solution was made by adding a few grams of NaCl to deionized water and measuring the conductivity with a conductivity probe. As this is a very low conductivity value, only a slight amount of NaCl needed to be added to 400-500 mL of DI water to make a batch of buffer. Often the actual measured conductivity fell between about 98 μS/cm and 102 μS/cm. Slight fluctuations in the conductivity value should have no effect on the DEP field.

The bead solutions were prepared by adding stock bead concentrate to the appropriate amount of buffer. The amount of actual bead solution used per experiment was kept at 20 mL. In other words, in all experiments, no matter the treatments, the volume of bead solution introduced into the chamber was kept constant. This kept the number of total number of beads introduced into the device constant. The dilutions of the beads used in these experiments are shown in Table 6.

Table 6 – Bead concentrations and dilution specifications for these experiments.

Bead Diameters	**Bead Dilutions**
6 μm beads	**42,000 beads/mL**
	0.020 mL stock bead solution (2.1 X 10^8 beads/mL)
	99.98 mL buffer
10 μm beads	**42,000 beads/mL**
	1.167 mL stock solution (3.6 X 10^6 beads/mL)
	98.82 mL buffer
10 μm beads	**36,000 beads/mL**
	0.2 mL stock solution (3.6 X 10^6 beads/mL)
	19.8 mL buffer

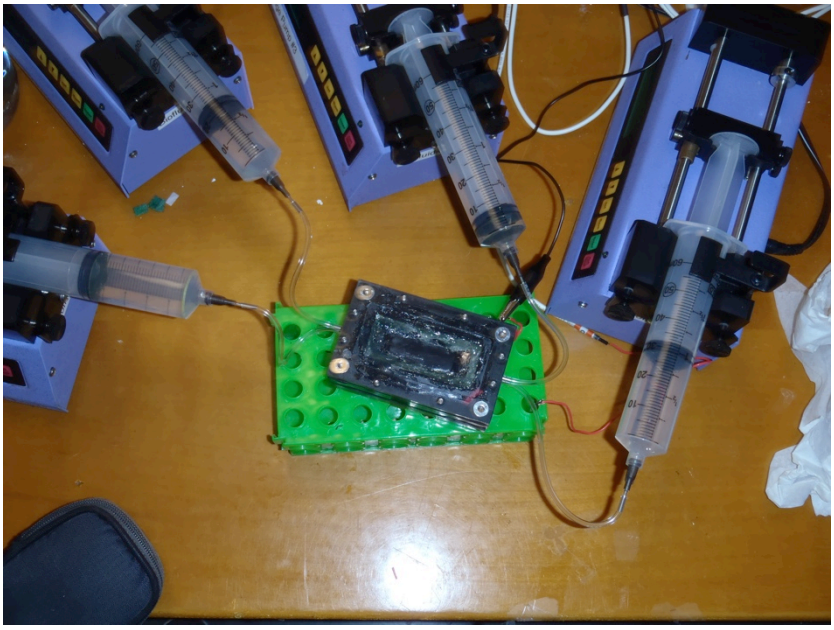

Figure 34 -- Image of the experimental set-up with the filtration device, four syringe pumps, and HVS leads.

Once the device was filled with buffer, all ports were connected as seen in Figure 34. Buffer fluid was pumped through the device, simply to check for leaks, proper syringe pump operation, and for the removal of any air trapped near the fluid connections, or other abnormalities. Once sound operation was verified, the device was ready for the suspension to be introduced. The top inflow syringe was then exchanged for a different syringe containing twenty milliliters of polystyrene bead solution. We

carefully exchanged these syringes, ensuring no large bubbles entered. In the future, this step should be replaced by the addition of a valve and a separate fluidic line for the suspension, so the syringe would not have to be exchanged each time suspension was introduced.

At this point in the experiment, immediately prior to the introduction of the suspension, the electrodes would be activated to the appropriate voltage. Of course, in the control treatments, no voltage was applied. However, in all other cases, the electrodes were connected and the software for the HVS was set to the appropriate value. The active lead from the HVS was connected to the top electrode above the filtration membrane and the ground electrode was connected to the bottom electrode.

The system was left to run for the short period of time that it took to introduce the twenty milliliters of bead solution. As this method of analysis requires the filtration membrane to be removed from the device before data is actually collected, the processes leading up to the removal of the membrane had to be carefully examined. The membrane removal is another aspect of the testing wherein those initial experiments helped develop much more consistent experimental practices. While the system was running and the polystyrene bead solution was being introduced, everything was monitored carefully for any problems. When the suspension inflow syringe approached the twenty-milliliter volume, both inflow pumps were quickly turned off and their syringes simultaneously disconnected. This step is critical because, if the pumps are turned off but remain connected, a vacuum in the device develops and the test is ruined. However, when the inflow tubing is disconnected air is allowed to enter the device and replace the fluid still being pulled into each outflow syringe. The system was left in this configuration until all

the fluid had been removed from the device. The device had to be cleared of fluid in order to remove the filtration membrane, as disturbing the membrane while still in contact with fluid would likely disrupt the particles that became adhered to its surface over the course of the test. Once the device was clear of fluid, the outflow pumps were turned off and disconnected and the device could be disassembled so the membrane could be placed on a slide for imaging.

The necessity of clearing the device of fluid could be quite problematic, as it is highly undesirable to alter the particles already deposited on the membrane. In some ways, introducing air into the device seems quite unpredictable. However, with this design, there are few alternatives for analysis. Also, as will be described in the Discussion section, the spread of particles over the surface of the membrane seemed fairly even, whereas if the influx of air affects the membrane, one might expect to see certain patterns in the spread of particles over the surface. In the initial trials, these kinds of patterns, which were seen as long streaks and lines of the fluorescent particles—obviously not evenly distributed--occurred presumably because of the air bubbles in the system. The difference between those initial experiments and the final experiments is that those initial air bubbles are entirely uncontrolled and affect the system during its filtration operation, while in the latter experiments, the influx of air should be relatively similar from test to test. Also, the suspension has already passed through the device, so maintaining the current state of the system is the only requirement. While it is likely this step does have some sort of effect on the particles on the membrane, those effects should be close to the same in all tests.

These methods also brought up questions concerning when exactly to turn off the electric field during tests when a voltage was applied. The field was kept active throughout the entire experiment, such that it was terminated when the outflow syringes were shut off. Thus, the goal was to keep the DEP force active while the remaining suspension was pulled out of the device. Conceivably, if the field were terminated earlier in the process when fluid remained in the device, some particles in solution could be pulled against the membrane that otherwise would have been repelled and collected in the retentate.

Markings on the filtration membrane were used to help guide the microscopy analysis of the membranes. Figure 35 shows a filtration membrane loaded onto a glass slide. This slide (from Test #19) shows how the markings delineated the areas of flow. A slightly yellow tinge can be seen in the flow quadrants due to the accumulation of fluorescent particles. In this case, the particles are yellow-green 10 μm particles, which were often visible on the filtration membrane.

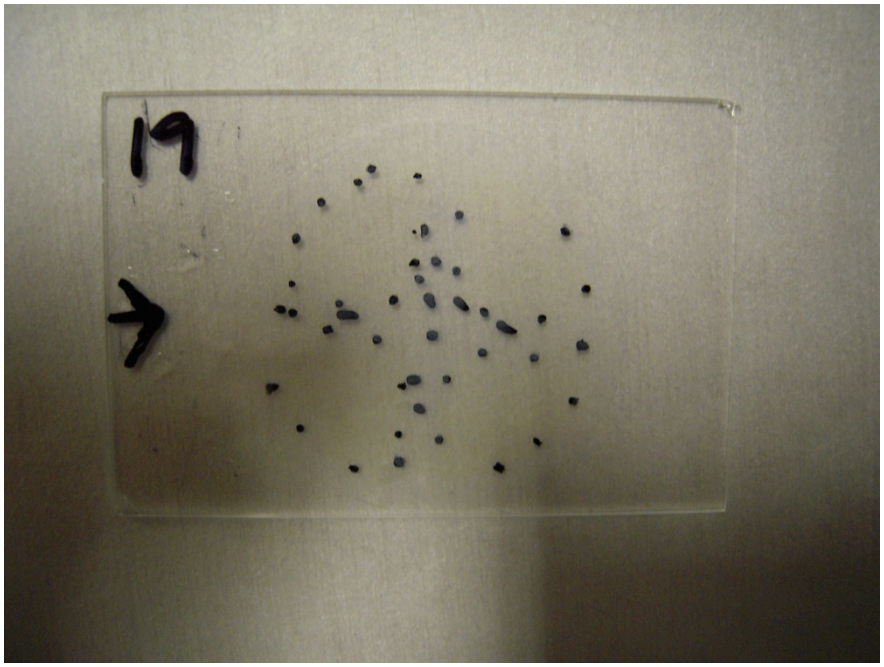

Figure 35 -- Image of a filtration membrane loaded onto a labeled glass slide. Note the markings on the membrane and the yellowish tinge over the flow quadrants.

After the filtration membranes were collected on slides for each experiment, we imaged them with the Olympus BX-41 fluorescent microscope at 10X magnification. This microscope, shown below in Figure 36, is coupled with a personal computer through a CCD camera and required software.

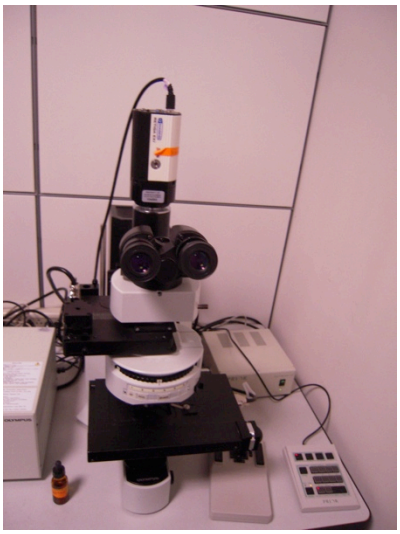

Figure 36 -- Olympus BX-41 upright fluorescent microscope used for the image analysis.

Four different quadrants in the images were analyzed in each filtration membrane. These quadrants can be seen in the image below, Figure 37. Five images per filtration membrane were recorded, and each was labeled based upon its test number and quadrant. The exact location of the image was chosen at random each time, with the only condition being that it lay within the bounds of the flow quadrant. The quadrants were labeled in order to compare different areas of the filter for differences in particles depositions. For example, intuitively one may suspect that Q2 and Q3 have higher numbers of particles deposited than Q1 and Q4, as Q2 and Q3 are located farther from the suspension inlet and the flow path may carry more particles through the "distal" area of the filter. The analysis of the particle spread over individual filter membranes is statistically paired test, as membrane quadrants are only compared against other quadrants on the same membrane, not across other membranes or tests. Results of such a test may inform us of whether the DEP force or the hydrodynamics affect the particle spread. If so, future designs, test parameters, and analysis techniques may need to be adjusted to account for this variation

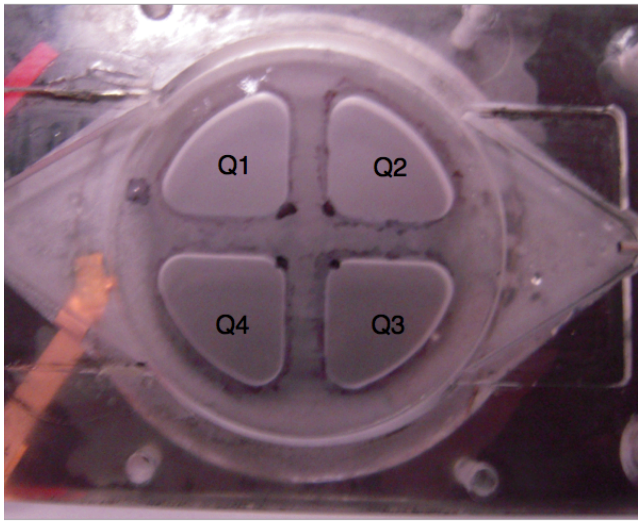

Figure 37 -- Image shows the quadrants of the filtration chamber and membrane.

After the images were recorded, it was important to develop an effective and efficient data analysis methodology. Initially, when processing the original data in the Spring 2011 trial experiments, *ImageJ* was used for particle counts. The images were simply processed by selecting a threshold and converting to binary, with dark background. From there, the "Analyze Particles" feature can be used to perform particle counts and percent coverage calculations. While this is an easy way to image a single image, it is time consuming when repeated several times. In the final set of experiments, a total of thirty tests were performed, recording five images per filtration flow quadrant, equaling six hundred images in total. Thus, a method to simplify and automate the particle counting process was highly desired. After a cursory review and research of MATLAB® image processing tools, a straightforward program was written that automatically loads the images, counts the particles, and outputs the results. The following screenshot, Figure 38, shows the code used to expedite the image analysis. The first lines of code import the images in the folder and the *for loop* performs the particle counts by reading in each image, converting them to binary, and performing the count.

```
 1 -    clear
 2
 3 -    FileList = dir('*.tif');
 4 -    N = size(FileList,1);
 5
 6 -    for k = 1:N
 7
 8          % get the file name:
 9 -        filename = FileList(k).name;
10
11
12 -         I=imread(filename); %load files
13
14            %figure,imshow(I); %shows each original image
15
16 -         I2=im2bw(I,0.02);
17
18            %figure,imshow(I2); %shows each black and white image
19
20 -         [L,num]=bwlabeln(I2,8); %location and particle counter
21
22
23 -         fprintf('%s %d\n',filename, num) %
24
25
26
27 -     end
```

Figure 38 – This MATLAB® code partially automates the particle counting in each of the image files of filtration membranes. This simple code reduced the time needed for image analysis tremendously.

Some parameters that had to be adjusted during the analysis were the inputs of the function on line 16 and 20. For the prior, this parameter quantifies the threshold level of the *im2bw* (binary 8-bit color to binary black and white) command. For some images, this value was set quite higher (meaning the threshold is less sensitive). However, in some cases, especially in blue 6 μm bead images, some areas of the membrane would be slightly out of focus and the beads not detected at higher threshold values. This was not usually a problem with the bright 10 μm yellow-orange beads. Some trial and error is required when setting the threshold value, as a too sensitive threshold will yield numerous artifacts and artificially inflate the particle count but a too large value may not be sensitive enough to detect some particles. The actual counting function, as seen in Line 20 of the screenshot, counts the number of connected objects, and is controlled by an input argument that defines the required number of connectivity. Thus, this version of

the program will detect objects in an 8-pixel connected neighborhood or greater. As both the 6 μm and 10 μm particles are much larger than 8 pixels in these images, this value remained the same throughout the analysis. The results were printed in the MATLAB® command window and copied over to Microsoft® Excel and Minitab® for data and statistical analysis.

The tests for the final experiments were performed in five sets. The following chart, Table 7, shows the parameters of each test. In each of the five groups, control and DEP treatments were applied.

Table 7 -- Parameters for the thirty tests in the final experiments.

Test #	**Bead Diameter**	**Flow Conditions***		
		$\mathbf{Q_{suspension}}$	$\mathbf{Q_{buffer}}$	$\mathbf{Q_{filter}}$
T1-T6, T11†	6 μm	8 mL/min	2 mL/min	6 ml/min
T6-T10	10 μm	8 mL/min	2 mL/min	6 ml/min
T12-T17	6 μm	10 mL/min	2 mL/min	8 mL/min
T18-T23	10 μm	10 mL/min	2 mL/min	8 mL/min
T24-T30	6 μm	8 mL/min	2 mL/min	6 ml/min

*$Q_{filtrate} = -Q_{suspension}$ and $Q_{retentate} = -Q_{buffer}$

†test performed separately, but conditions were equivalent

5 Results

We recorded trace measurements from the Labsmith® HVS™ of the non-control tests which are summarized in Table 8. This verifies the electrodes were operating at the expected potentials and resultant currents. A sample of the raw output from the HVS can be seen in Appendix D. The raw data of the averages and standard deviations below is consists of the entire data set of one test at the specified potential. The standard deviations show the potentials induced by the HVS fluctuate considerably, but the average of the values is closely centered around the expected value. Also, because the voltage fluctuates instantaneously, the resultant current values are distributed over a large range. This fluctuation, which was not expected or observed until after the tests were complete, is not accounted for in the COMSOL™ model. According to the Labsmith HVS™ literature, the output can be excessively noisy at voltages lower than 100 V. Appendix D shows a sample of the raw HVS data and supplementary analysis, with complete data sets organized into histograms.

Table 8 -- Displays overview of electrical measurements experiments where electrodes are active. The leftmost column is the programmed (expected) voltage value.

	VOLTAGE (VOLTS)		CURRENT (μA)	
HVS Setting (DC)	Average	Standard Deviation	Average	Standard Deviation
3V	3.031	4.287	0.159	0.455
5V	5.099	5.641	0.157	0.667
6V	6.101	6.250	0.160	0.770
9V	9.005	7.519	0.140	1.010
12V	12.104	10.091	0.114	1.329
15V	14.967	8.276	0.185	1.257
20V	17.611	10.158	0.226	1.214

Qualitative differences in observations are readily apparent. Most tests have particle spreads that appear distributed uniformly as in Figure 39, while a few lack particles almost altogether as seen in Figure 40, and some seem to have aggregations of particles, such as the 10 μm beads in Figure 41.

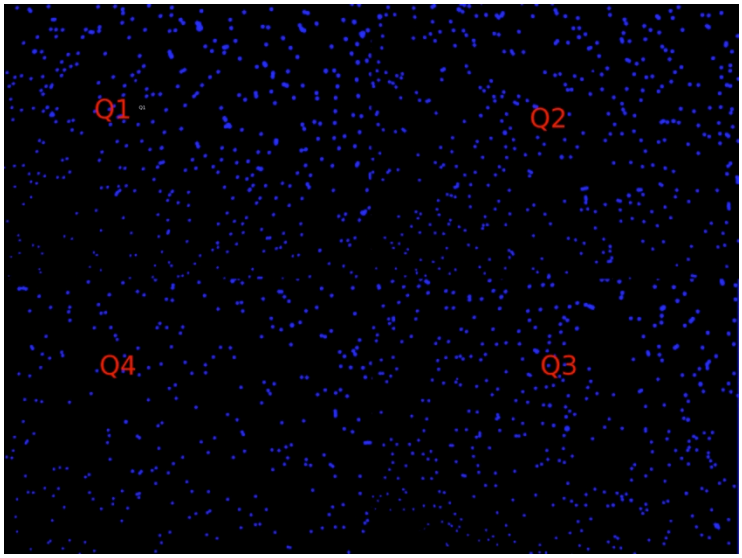

Figure 39 -- A set of images from Test-02, which is a characteristic representation of the filtration membrane with no active DEP field.

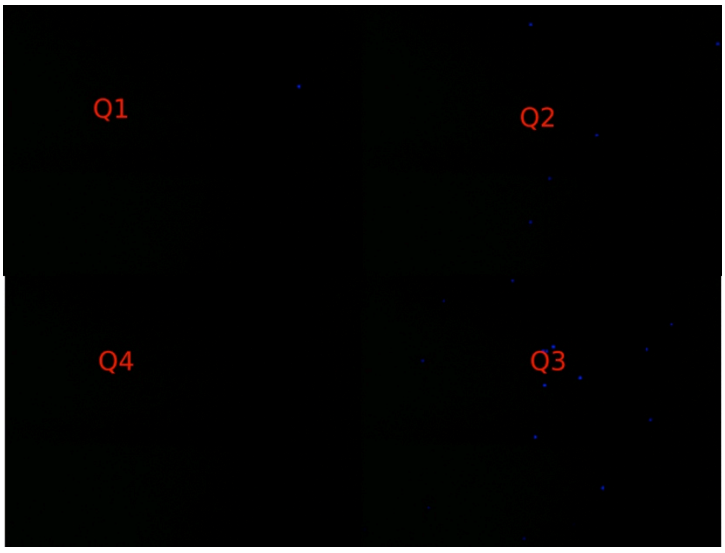

Figure 40-- Image of filtration membrane of Test 13, a control. This test was likely problematic, as barely any particles were present on the membrane surface.

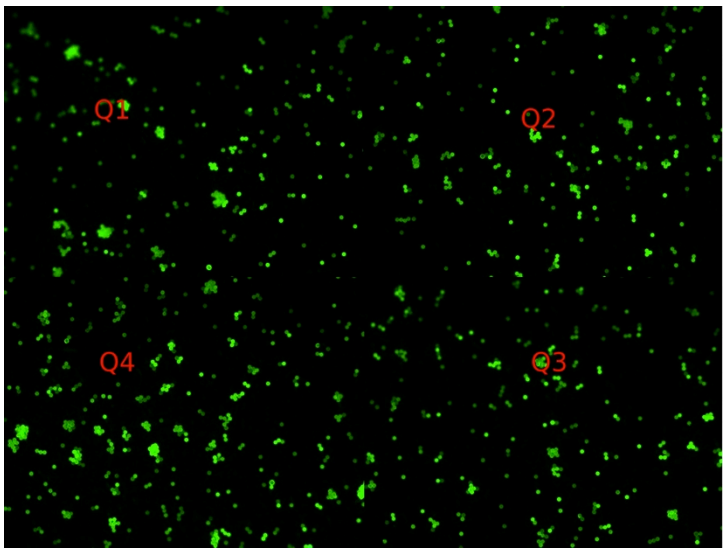

Figure 41 -- Montage of Test-18 filtration images, showing the yellow-green 10 um particles.

As the images were processed, the binary images produced from the original 8-bit color images were monitored to ensure a valid representation of the number and size of particles. The image below, Figure 42, shows an example of this conversion. As described in the Methods section, some trial and error was used until the right threshold value was obtained.

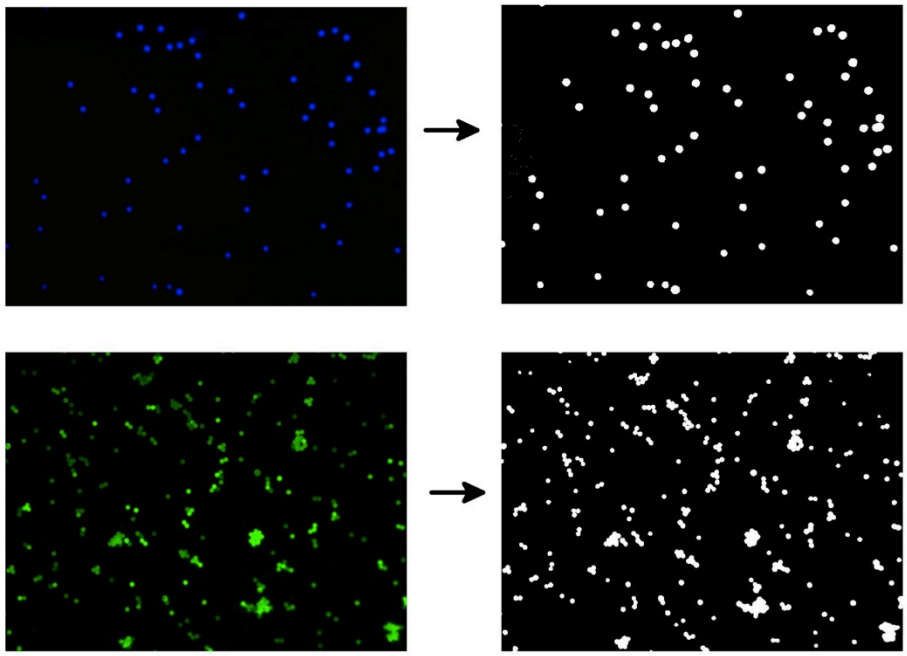

Figure 42 -- The figure above shows one example of the unprocessed 8-bit color images with the corresponding binary image, after MATLAB™ processing. Threshold values were larger for the 10 μm yellow-green beads on the lower panel.

From a statistical perspective, three predictor variables (electric field, particle size, flow rate) have been manipulated during these tests, each potentially affect a response variable of the number of particles per field of view at 10X magnification. If the beads are distributed relatively evenly across the membranes, this response should be an adequate proxy for the number of beads per filtration quadrant, or per entire filtration membrane.

Clearly, from the information presented thus far, the main effect we are interested in testing is the relationship between the electric field strength (via applying voltage to electrodes) and the number of particles accumulated on each membrane. Often, because both of these variables are numeric, a linear regression would be used to test for a correlation. However, our understanding dictates that the voltage levels should be analyzed in a categorical fashion, as a linear relationship may not represent the response

well. Specifically, when the hydrodynamic forces outweighs the DEP force, we expect little difference in particle counts than the control, as the particles will likely still settle on the filtration membrane surface, perhaps only more slowly. Conversely, when the DEP force outweighs the hydrodynamic force on particles, the particles will likely be swept away and captured in the retentate. In other words, there is a critical level, where the forces are predicted to balance out, and at some value close to this threshold, we expect a step in a plot of values. Perhaps, the curve prior and the curve following this incontinuity could be regressed (linear or higher order) separately, but the entire curve is not expected to be continuous. For this reason, ANOVA and related statistical methods have been applied to the data. Detailed analysis of response curves should be considered for future projects, but are out of the scope of this project and data set.

Because our goal is to test the factor levels (voltages) that reduce the particle count significantly, as compared to the control, we used the Dunnett's Test, a type of ANOVA, which compares individual treatment means to the control mean. This method has more power than a basic ANOVA, as fewer tests are performed and more degrees of freedom retained.

The following table shows an excerpt of the Dunnett's test over all the tests, wherein differences in particle count are tested against the control of zero voltage. At the 5% overall significance level, this test does not indicate a significant decrease in particles, when exposed to voltages at or above the predicted threshold value.

Table 9 -- Dunnett's statistical test of all factors and factor levels against their respective controls.

```
Dunnett 95.0% Simultaneous Confidence Intervals
Response Variable ParticleCount
Comparisons with Control Level
Voltage =  0  subtracted from:

Voltage   Lower  Center  Upper  -------+---------+---------+---------
 3       -512.1   -53.1  405.9  (--------------*---------------)
 5       -244.7    -6.0  232.7           (-------*-------)
 6       -436.1    22.9  481.9    (---------------*--------------)
 9       -340.2    -7.9  324.5        (----------*----------)
12       -249.2   -32.8  183.7           (------*------)
15       -287.9   -51.4  185.1         (-------*-------)
20       -488.9  -172.5  143.8   (---------*----------)
                              -------+---------+---------+---------
                                  -300         0       300
```

The following Minitab® output, Table 10, shows the results for a Dunnett's test for the subset of 6 um particles and 6mL/min experiments at the 5% experimentwise (overall) significance level. The Dunnett's test controls for Type 1 error, such the individual alpha value is equivalent to the overall value divided by the number of tests.

Table 10 -- Dunnett's statistical test for 6 μm particles at Q_mem = 6 mL/min, at the 5% overall significance level.

```
Dunnett's comparisons with a control

Family error rate = 0.05
Individual error rate = 0.0144

Critical value = 2.96

Control = level (0) of v2

Intervals for treatment mean minus control mean

Level   Lower  Center  Upper  ---+---------+---------+---------+------
 5     -387.1   -56.1  274.8          (------------*------------)
12     -424.3  -137.6  149.0        (----------*-----------)
15     -568.6  -237.7   93.3  (------------*------------)
20     -577.7  -246.7   84.2  (------------*------------)
                             ---+---------+---------+---------+------
                             -500      -250         0       250
```

Because the Dunnett's test at the 5% overall significance level reduces the chance of finding "false" differences, it correspondingly reduces the power to find actual differences. Since our dataset is already lacking in statistical power, we performed the

Dunnett's comparison using the individual significance value of 5%. While this assumption is not a statistically valid approach, we feel that it is an appropriate measure, considering our data set and the stage of development of the device.

Table 11 -- Shows the same Dunnett's comparison as Table 10, after increasing the family error rate such that the individual alpha value is 5%.

```
Dunnett's comparisons with a control

Family error rate = 0.2
Individual error rate = 0.0628

Critical value = 2.09

Control = level (0) of v2

Intervals for treatment mean minus control mean

Level   Lower  Center  Upper  ----+---------+---------+---------+-----
 5     -290.4   -56.1  178.2           (-----------*-----------)
12     -340.5  -137.6   65.3         (---------*---------)
15     -471.9  -237.7   -3.4  (-----------*-----------)
20     -481.0  -246.7  -12.5  (-----------*----------)
                             ----+---------+---------+---------+-----
                              -400      -200         0       200
```

The Dunnett's test above shows the 15 V and 20 V treatment levels are significantly different (less than) the control level, as the intervals of the treatment mean minus control mean do not include zero.

A simple representation can be seen in Figure 43 that summarizes these results and reinforces the above statistical analyses. The variance in each of the controls is large, which is a violation of the constant variance assumption, which is required for statistical tests such as ANOVA and linear regression. In this dataset, this unequal variation is probably due to a lack of sufficient repetition, but small standard error values make sense for the 15 and 20 V treatments, as the particle counts are so small.

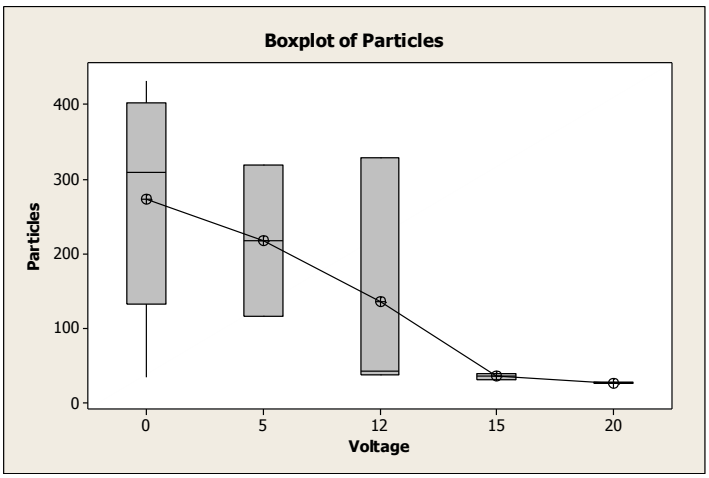

Figure 43 – Boxplot representation of the number of particles per field of view at a 6 mL/min filter flow rate

6 Discussion

The Results section focuses on 6 μm particles tested because we deemed that subset of the experimentation more successful than the other tests. On initial analysis, all other tests showed none of the expected correlations that the 6 μm / 6 mL/min tests showed. After consulting notes taken during experimentation, the top electrode likely did not have a robust connection during Tests 7 through 23. While preparing to perform Test 7, the connection for the top electrode was broken, and then presumably not repaired correctly. Not knowing that the repair was unsuccessful, we performed Tests 7 through 24 without further modification of the device or alteration of the electrode.

After some initial analysis of those tests showing no expected correlations, we reinforced the electrode connection. At this point, we attempted to replicate the initial 6 μm / 6 mL/min results found in Test 1 through 7. Because these tests were successfully replicated in Tests 24 through 30, we expect the electrode connection did fail during the

intermediate tests (Test 8 through 23). Additional statistical analyses and plots of the full data set, including the likely faulty tests, are provided in Appendix E.

The successful replication of the 6 μm / 6 mL/min results is the capstone of the experimental validation of the project. We met our goals through the design, fabrication and validation of the device. Through future projects, more detailed theoretical predictions, revised and improved designs, and more powerful testing protocol should be performed. Future work aimed toward the improvement of this device will be discussed more in the Conclusion section that follows.

The scope of this project dictates simple validation techniques aimed toward establishing whether or not the expected function of the device is plausible. While the successfully replicated data set demonstrated promise, several factors add uncertainty and difficulty, and ultimately increase the error in the experiments. Many of these factors are intrinsic to the device design, the most notable of which is the 12-bolt design used to secure the perimeter of the device. Because the device must be nearly fully assembled and disassembled for each test, individual tests took 30-45 or more minutes, not including imaging. Also, the way in which the fluidics of the device are set up, changing input and output syringes requires significant time and energy.

Because the current design does not allow for *in situ* imaging and data gathering, there exists no real-time representation of the filtration. Furthermore, each time the device and membrane is handled in between testing and data gathering invites more risk of altering the data. While this error is random and should not bias the results, it adds to the overall variance in the data, which makes proving the effectiveness of the device that much more difficult.

The inconsistencies with the Labsmith™ HVS™ must be noted. (Further analysis of the generated voltages can be found in Appendix D.) Because the HVS™ did not produce steady DC potentials, as the theory and experimental set-up dictates, additional caution must be taken when drawing inferences from the results. The chance that the noise in the signal affected the results is likely, although we cannot confidently estimate the magnitude of any such effects. However, based on the frequency of oscillation (on the order of tens of Hertz), it is likely the DC effects elicited by the device were similar to a pulsed DC design. Many researchers have used pulsed DEP to translate particles and disaggregate filter cakes, which suggests this device may be capable of particle levitation and removal in either pulsed or steady modalities. Having said that, this discrepancy should be remedied (and pulsed versus steady modalities tested) in the future with a simple and predictable low-voltage DC source.

Other design attributes, from the electrode sizes and geometries to the channel and chamber designs, really have not been compared to other possible designs in a regimented theoretical or experiential fashion. As a prototype, much of the developmental motivations were drawn from basic logistical challenges, not critical evaluations of its functions. As such, significant improvements, modifications, and applications of the device may be accomplished in the future.

7 Conclusion

Future work involving projects similar to that presented in this thesis will need to focus efforts on the theoretical predictions and modeling of the device. Using the experience of this project, software and mathematical models may be used to better

approximate and understand the physics and fluid mechanics of the device. Iterations of these models will lead toward more sophisticated development of the filter housing and assembly, as the iterations will continually improve the filtration mechanisms.

Some specific ways that the software models should be improved upon is to first develop 3-D multiphysics models. The current 2-D models are only approximations and the assumptions associated limit their accuracy and usefulness. However, transitioning into full dimensional models is not a trivial task, as the computational power required increases substantially. Average computers would likely not have enough memory and computing power to process the additional nodes in the mesh of the 3-D models, but a creative model design and mesh can reduce the complexity of the mesh, such that it can be computed with readily available computers. Taking advantage of geometric symmetry and other simplifications may make a sophisticated model less computationally expensive.

After the individual fluid and DEP models are enhanced and validated, the next logistical advancement is the combination of the models and the introduction of the particles. COMSOL™ provides the capability to combine numerous different physics modules in one overarching model. For example, a future combined model may include the Stoke's Flow and Steady State DC physics modules. A fully integrated model will allow for the modification of several different variables, resulting in the ability to test the effects of particle sizes, flow rates, voltages, and channel and electrode geometries in less time.

Some seemingly basic attributes of the device that will be modified are the chamber and channel geometries, and their corresponding flow rates. The geometry of

future generations of the device may diverge, with one group aimed toward biofluid sample pre-processing and separation (likely to trend toward microfluidic diagnostic instruments), while a second group may address the needs and limitations of the current clinical gold standard of dialysis devices and other blood processing technologies, where large volume, but efficient process must be performed. Whether large or small samples are to be processed by future devices, the geometries of the device not only affect the hydrodynamics, but also the behavior of the electric field, as the electric field streamlines bend around the non-conducting materials of the housing and thus create the gradient and DEP force.

Because the future goal of the device is not only to reduce filtration membrane fouling, but also enhance the separation, the integrated model should be tested with multiple particle diameters. As the bench top testing and validation of the separation of a bimodal suspension (i.e. 10 μm particles and 1 μm particles) is complex, the development of more sophisticated models is paramount to advancing the design.

Another interesting test hypothesis and goal, which is actually a preliminary to any tests with bimodal suspensions, is to show that larger scale particles can be "filtered" even when the diameter of the membrane pores are larger than the particle diameter. In this situation, the particle is levitated and flushed away via the same DEP force and cross-flow filtration techniques discussed thus far. However, because the filtration pore diameter can be increased, the pressure gradient across the device is reduced, while the filters still performs an equivalent or possibly enhanced separation compared to cross-flow filtration with the standard pore size and no DEP field. In fact, because the pressure gradient can be lowered, smaller, more energy efficient pumps may be used in the

systems. Hence, not only are manufacturing costs be reduced, but also the operational costs of such systems may be reduced, as the systems are designed to be lower maintenance, require fewer disposable parts (e.g., replacement of filtration membranes), and require less power. In parts of the world where electricity is still limited, the reduction of power demand in clinical equipment could greatly increase the availability. Certainly, the reduction in energy consumption reduces cost in the developed world as well.

Future work must also consider advancements in experimentation and validation that will lend information not only toward whether the device is working as expected, but also how the device is accomplishing its defined objectives. This line of testing will likely involve advanced imaging analysis techniques such as flow visualization and *in situ* fluorescent video microscopy, flow cytometry for particle counts in retentate and permeate.

The opportunities for future development of technologies such as this thesis project extend well beyond simple filtrations and separations. If these techniques progress toward healthcare technologies, such as dialysis and diagnostic systems, the research in this field will increase substantially.

Efficient and inexpensive devices will likely gain ground in the future years as the fundamental healthcare disparity between the developing world and other nations remains immense. Furthermore, increasing financial constraints will likely put pressure on Western style healthcare to reduce costs and increase efficacy. This project investigated an area that has the potential to benefit many health care technologies and improve the accessibility and quality of diagnostics and treatments worldwide. This theory and

prototype have undergone a preliminary validation, which indicated a notable decrease in filter fouling, increase in specificity and efficiency, all through an inexpensive and easily fabricated device. We are encouraged by the results presented thus far and look forward to further development of this prototype in the future.

Appendix A DC DEP and Flow Calculations

Variables:

$F_{\mu} = [N]$ hydrodynamic force

a = [m] particle radius

$\varepsilon_f = [\frac{F}{m}]$ fluid permittivity,

where $\varepsilon_f = \varepsilon_r \varepsilon_0$

ε_r = relative permittivity

$\varepsilon_0 = \left[\frac{F}{m}\right]$ absolute permittivity

$U_{ave} = [\frac{m}{s}]$ average velocity

$\nabla|E|^2 = [\frac{m \cdot kg^2}{s^6 \cdot A^2}]$ electric field gradient

$\mu = \left[\frac{N \cdot s}{m^2}\right]$

Expressions:

Eq. (14) -- Hydrodynamic force expression for a spherical particle

$$F_{\mu} = 6\pi a \mu U_{ave} \quad \textbf{(14)}$$

Eq. (15) -- DEP force exerted on spherical particle

$$F_{DEP} = -2\pi\varepsilon_f a^3 \nabla|E|^2 \quad \textbf{(15)}$$

Eq. (16) -- Force balance of hydrodynamics and DEP

$$6\pi a\mu U_{ave} = -2\pi\varepsilon_f a^3 \nabla|E|^2 \quad \textbf{(16)}$$

Eq. (17) -- Rearrangement of Eq. (16) to solve for the resultant velocity

$$U_{DEP} = \frac{-2\pi\varepsilon_f a^3 \nabla|E|^2}{6\pi a\mu} \quad \textbf{(17)}$$

Eq. (18) – Simplification of Eq. (17)

$$U_{DEP} = \frac{-\varepsilon_f a^2 \nabla|E|^2}{3\mu} \quad \textbf{(18)}$$

We solved for the average fluid velocity flow through each pore based upon the volumetric flow rates through the device, the results of which are demonstrated in Figure 8. Using the total volumetric flow through the membrane Q_{filter}, we found the expected flow velocity by adapting the basic flow relationship seen in Eq. (19). For the area term,

we calculated the "void area" of the filtration membrane by summing the area of each pore.

Eq. (19) -- Volumetric flow relationship (fluid velocity times cross-sectional area equals the volumetric flow rate)

$$Q = VA \tag{19}$$

Using the available area of the filtration membrane, the total area of the all the pores can be calculated via the porosity, as shown in Table 12 below.

Table 12 -- Values used to calculate an example pore velocity.

Pore Velocity Calculation		
Area	0.00144207	m^2
	14.4207	cm^2
epi	0.1	
flux_area	1.44207	cm^2
Q_mem	6	ml/min
v_ave	4.160685681	cm/min
	0.069344761	cm/s
	0.693447614	mm/s

Eq. (20) – Calculated average velocity through each pore, as calculated from the values in Table 12

$$Pore\ velocity = 0.0001Q_{filter} \quad \textbf{(20)}$$

Eq. (21) – Calculated average velocity due to DEP force

$$U_{DEP} = -1.13X10^{-7}(a^2)\nabla|E|^2 \quad \textbf{(21)}$$

Assume: Particle levitates when Pore velocity = $-U_{DEP}$

By combine the two previous equations, we can solve for an expression of the levitation relationship, wherein the hydrodynamic and DEP forces are opposite and balanced. Graphically, the curve generated from the following equations displays a threshold, where, on one side of the curve, the hydrodynamic forces dominate, while on the other side, the DEP dominates and particle repulsion occurs.

Eq. (22)

$$0.0001Q_{filter} = -1.13X10^{-7}(a^2)\nabla|E|^2 \quad \textbf{(22)}$$

Eq. (23)

$$\nabla|E|^2 = \frac{0.0001Q_{filter}}{-1.13X10^{-7}(a^2)} \quad \textbf{(23)}$$

Note that we derived the electric field gradient values from the COMSOL™ model, as seen in Figure 5 in the body of the document. The following chart,

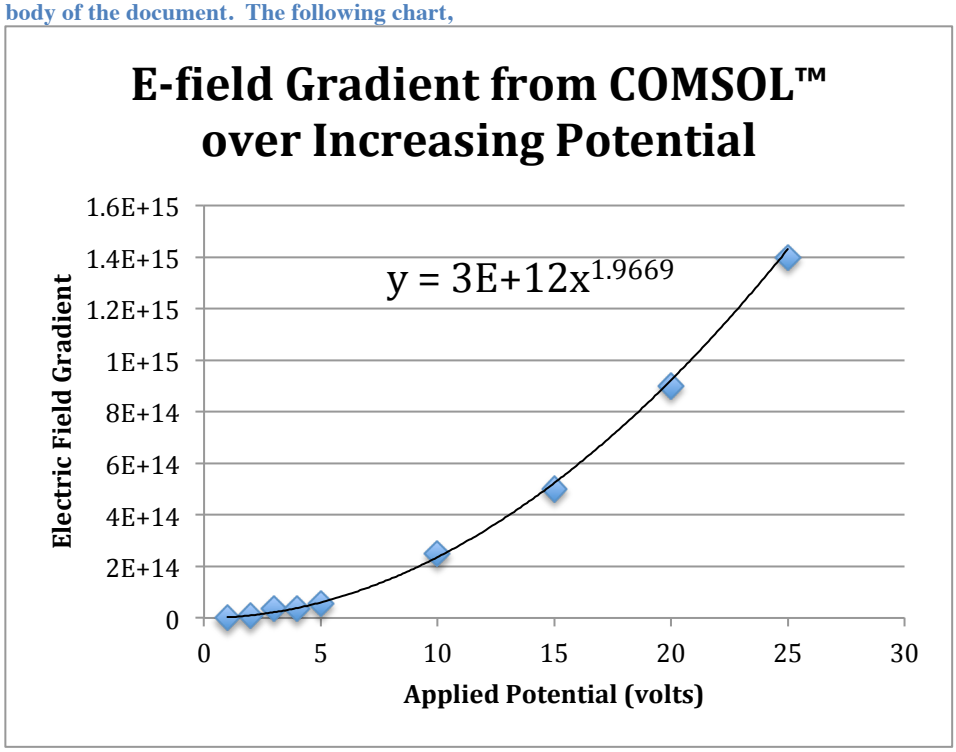

Figure 44, shows the relationship between the potential applied to the electrodes and the electric field gradient. From this plot, we can generate the follow equation.

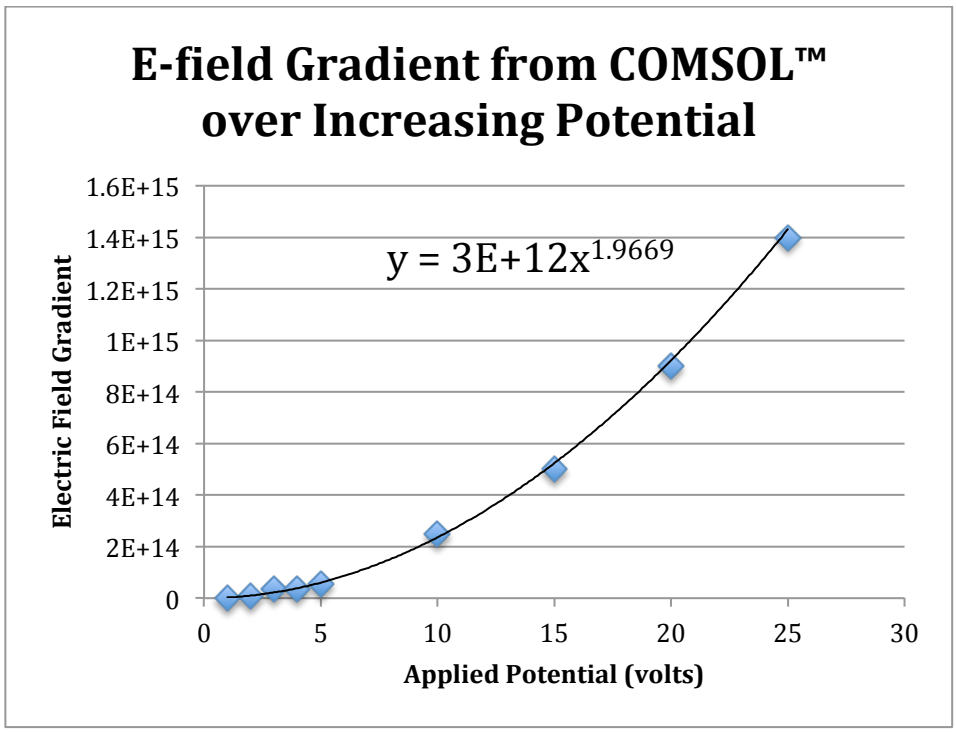

Figure 44 -- Plot of the electric field gradient versus applied potential, calculated from the COMSOL™ electric field model.

Eq. (24) -- Electric field gradient dependent on applied potential

$$\nabla|E|^2 = (3\ X\ 10^{12})v^{1.9669} \qquad \textbf{(24)}$$

where v is the applied potential in volts

Substituting this expression into Eq. (25) allows us to express these conditions in the two parameters that we have direct control over in the experiment: the electrode potential (via the HVS) and the volumetric flow rate (via syringe pumps).

$$(3\ X\ 10^{12})v^{1.9669} = \frac{0.0001Q_{filter}}{-1.13X10^{-7}(a^2)} \quad \textbf{(25)}$$

Eq. (26) – Solve for voltage in terms of flow rate and particle radius

$$v = 0.0000142794(\frac{Q}{a^2})^{0.508414} \quad \textbf{(26)}$$

Appendix B CNC Instructions

1) Use MasterCAM to program all tool paths, settings, origin, cut depths, and feed speeds, spindle speeds, rough cuts, and finishing cuts.
2) Load part into vise and make sure it is aligned and secured by tapping with rubber mallet.
3) Measure tool lengths and find the edge of the part using the industrial ruby and Renishaw tool setter device.
    a) Must align part to within 0.4" of edge to be measured
    b) Push "edit," then "Program Conversions" three times
    c) Select "Orientation" and enter "54"
    d) Select "Add to MDI"
    e) Push "Cycle Start"
4) Machine will align and measure edge of part
5) Edge must be found each time part is moved or new part is installed into machine
6) Load chucks into mill
    a) Select "T#", "Enter", APC Forward (Beware of moving parts as machine switches tooling
7) To measure tool length, use the Renishaw contact tool setter
    a) This device automatically adjusts for tool length offset for each tool
8) Then, copy file from thumbdrive.
9) At this point, the CNC should be set up for machining. However, before machining it is good practice to run entire operation several inches above the part to be machined,

thus establishing a “dry run” where one can make sure all operations are performed as desired.

10) Things to check for during the “dry run” include

    a) Correct position of lead-in

    b) Correct tool in spinde

    c) Reasonable feed speed

    d) Correct tooling changes

11) After carefully reviewing all parameters and simulation, return the offset to zero to perform actual cycle and press start.

Appendix C Engineering Drawings

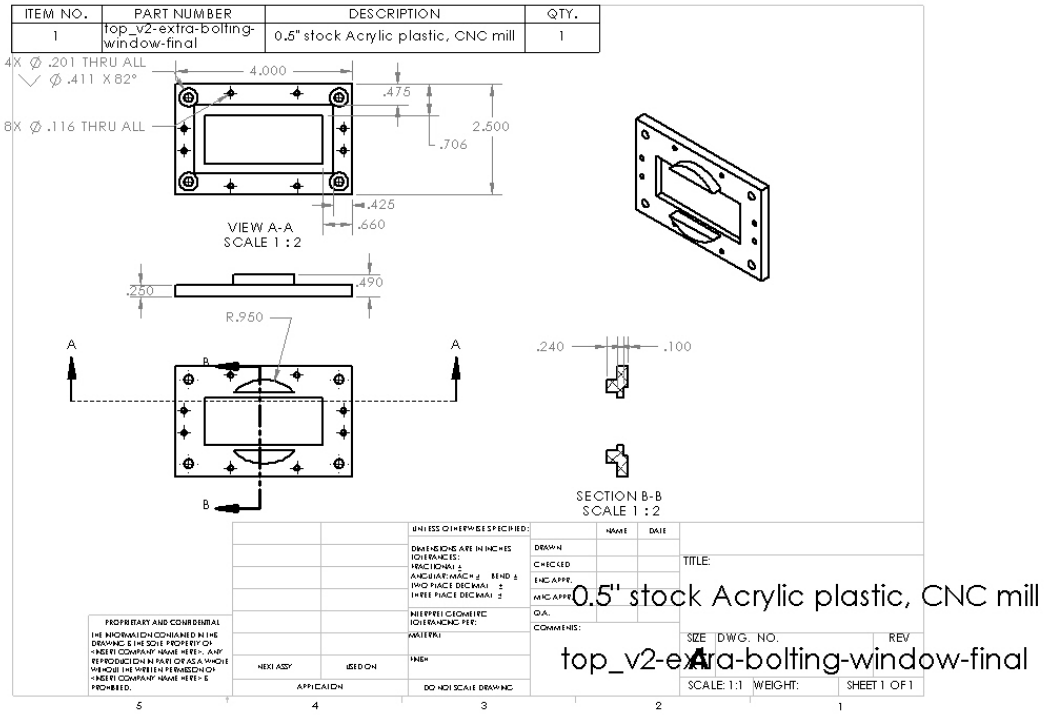

Figure 45 -- Engineering drawing of the top part of the chamber.-

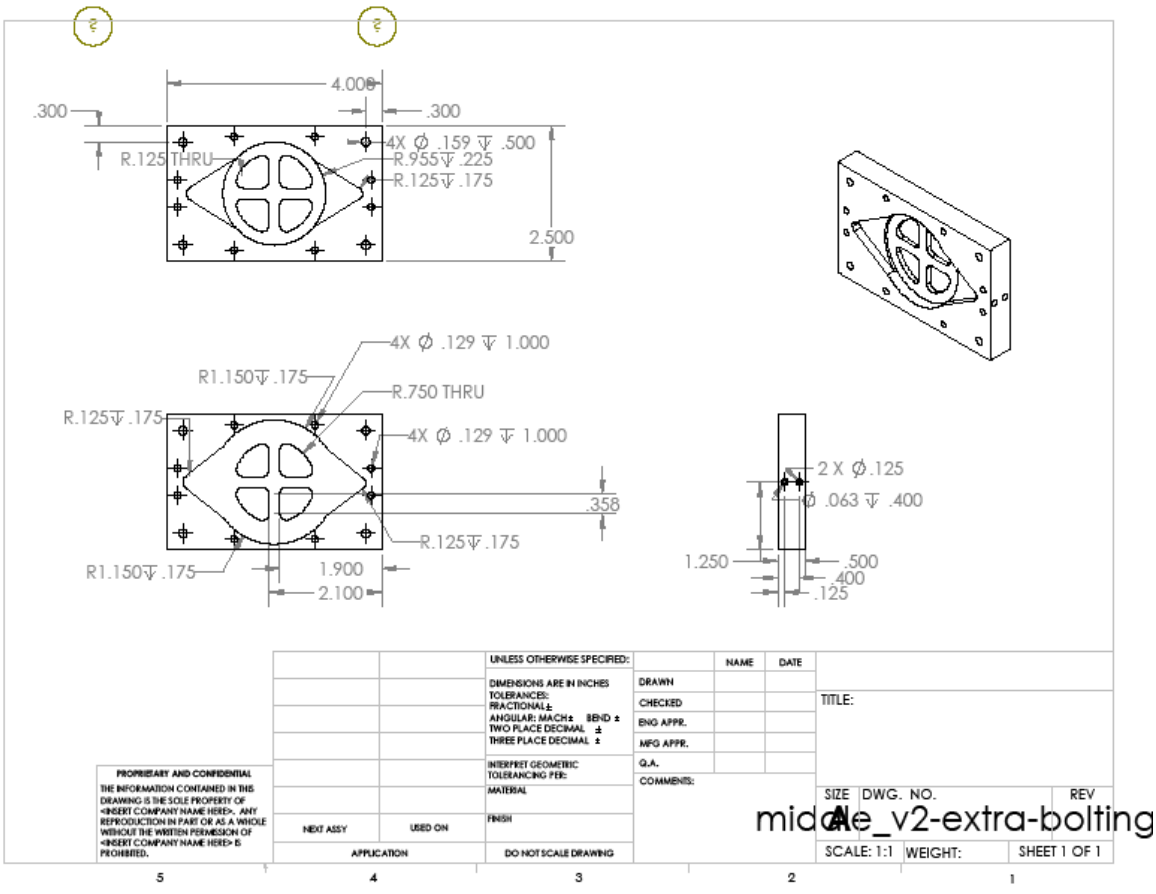

Figure 46 -- Engineering drawing of the middle part of the chamber.

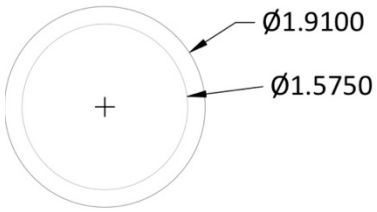

Figure 47 – AutoCAD sketch of the washer part, which helped to secure the filtration membrane.

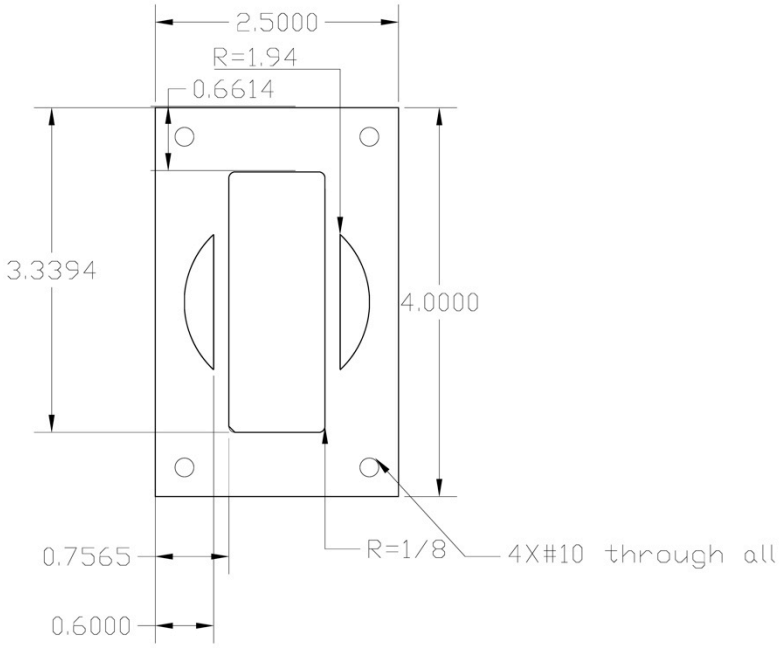

Figure 48 -- AutoCAD sketch of the gasket used to seal the top part, window, and middle part of the chamber.

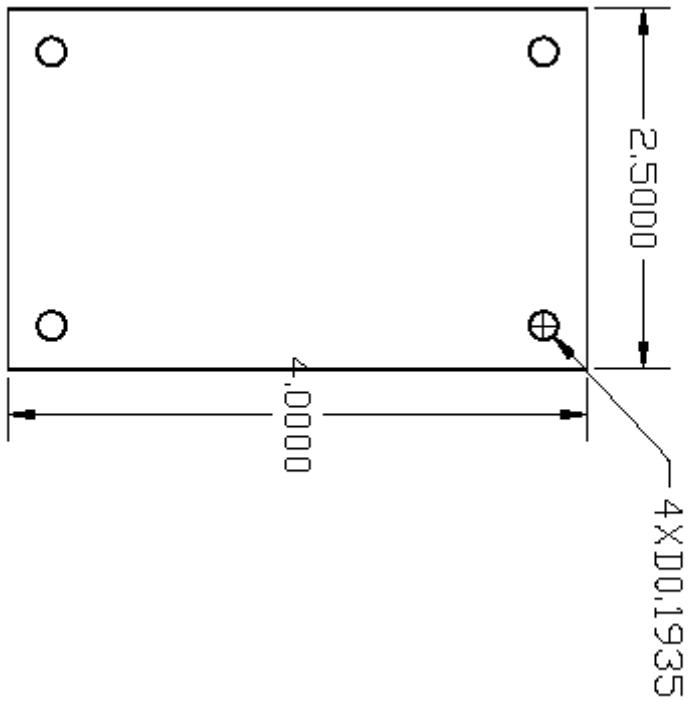

Figure 49 -- AutoCAD drawing of the bottom gasket, which sealed the middle and bottom pieces of the chamber.

Appendix D Sample Data Recording from HVS

The following table shows a sample recording of the values recorded from the Labsmith® High Voltage Sequencer. The data values are measured at 16 Hz, as can be seen in the time increments of 0.0625 seconds. The data shown is only a 3 second subset of one test, wherein the equipment was set to apply 12 volts DC to the electrodes. The recorded voltages range roughly from zero to twenty volts at individual time points. The average of all the individual voltage values is 12 volts and the average of the individual currents in the test below is 0.11 μA.

Table 13 -- Sample data recording from the Labsmith® HVS consisting of the time, voltage, and current values for a test set at 12 volts DC.

time (s)	Ch. C Voltage (V)	Ch. C Current (uA)
0	0.351	0.04
0.063	19.52	0.27
0.125	4.028	-2
0.188	12.073	2.35
0.25	16.123	-1.63
0.313	0.17	0.04
0.375	20.402	0.11
0.438	0.113	0
0.5	19.836	0.19
0.563	6.256	-2.02
0.625	8.481	2.26
0.688	19.857	0.1
0.75	0.368	0.04
0.813	19.368	0.23
0.875	0.398	-1.8
0.938	16.114	2.48
1	19.426	0.12
1.063	1.778	1.22
1.125	20.237	0.12
1.188	0.188	0.08
1.25	19.813	0.01
1.313	18.584	0.08
1.375	12.151	2.44

1.438	19.691	0.02
1.5	0.32	0.08
1.563	19.261	0.14
1.625	-0.135	-0.17
1.688	19.603	2.5
1.75	19.442	0.09
1.813	6.25	2.19
1.875	19.993	0.2
1.938	0.272	0
2	19.794	0.1
2.063	16.354	-1.51
2.125	18.083	2.45
2.188	19.229	0.04
2.25	2.85	1.7
2.313	19.088	-0.01
2.375	12.435	-2.04
2.438	20.522	0.73
2.5	19.312	0.04
2.563	9.049	2.32
2.625	19.915	0.09
2.688	-0.146	-0.67
2.75	19.644	0.1
2.813	13.084	-1.82
2.875	20.037	1.07
2.938	19.025	-0.03
3	0.054	0.22

Figure 50 below shows histograms of values recorded from the HVS™ . The HVS™ does not seem to apply smaller voltages in a constant, even fashion. The standard deviations from Table 8 in the body of the document suggest the data is highly spread, and the histograms below confirm this observation. In fact, the histograms show the HVS™ does not excite at the lower voltage levels, but will excite at much higher levels for a small fraction of the time. These values, once averaged over the whole of the active time period, are "diluted" by many "zero voltage" time points. In other words, if 12 volts is programmed, the device might alternate between 0 and 24 volts.

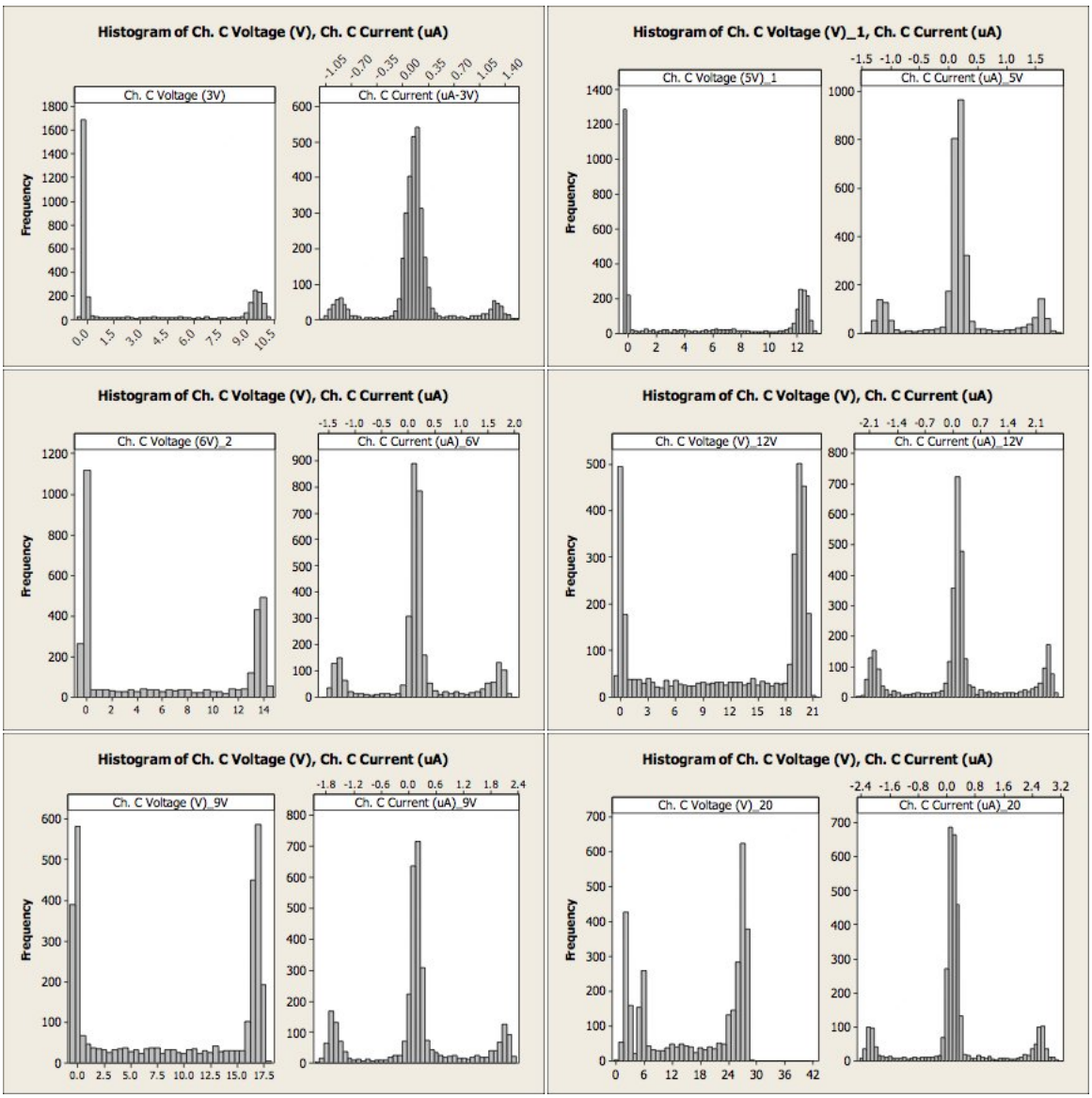

Figure 50 -- This image is a montage of histograms from six different tests with active electrodes. Note the bimodal spread of values for the voltage measurements.

The relationship between the voltage and current histograms in Figure 50 shows the "alternating" DC results in three prominent current groupings. The largest current grouping likely corresponds to the "programmed" or desired voltage, and the two small groups on either side likely result from each peak and trough of the voltage signal.

Appendix E Other Results

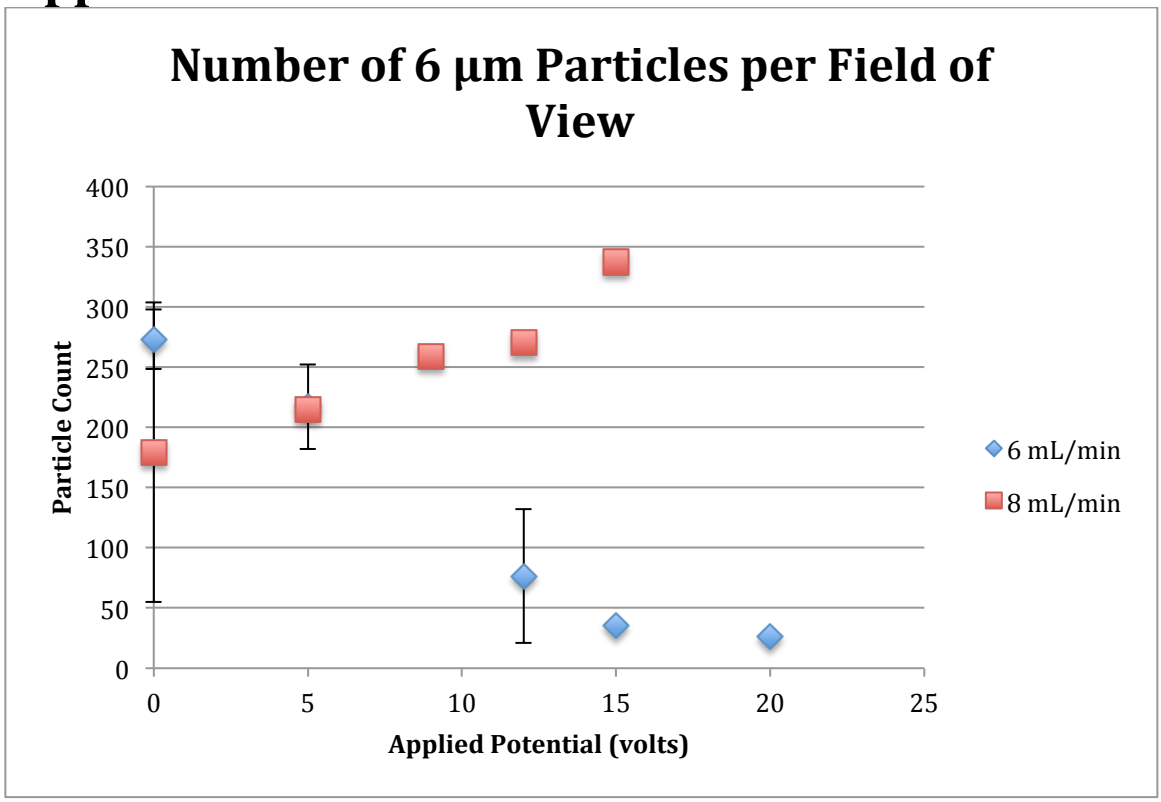

Figure 51 -- Plot of counts of 6 μm particles at both tested filtration flow rates.

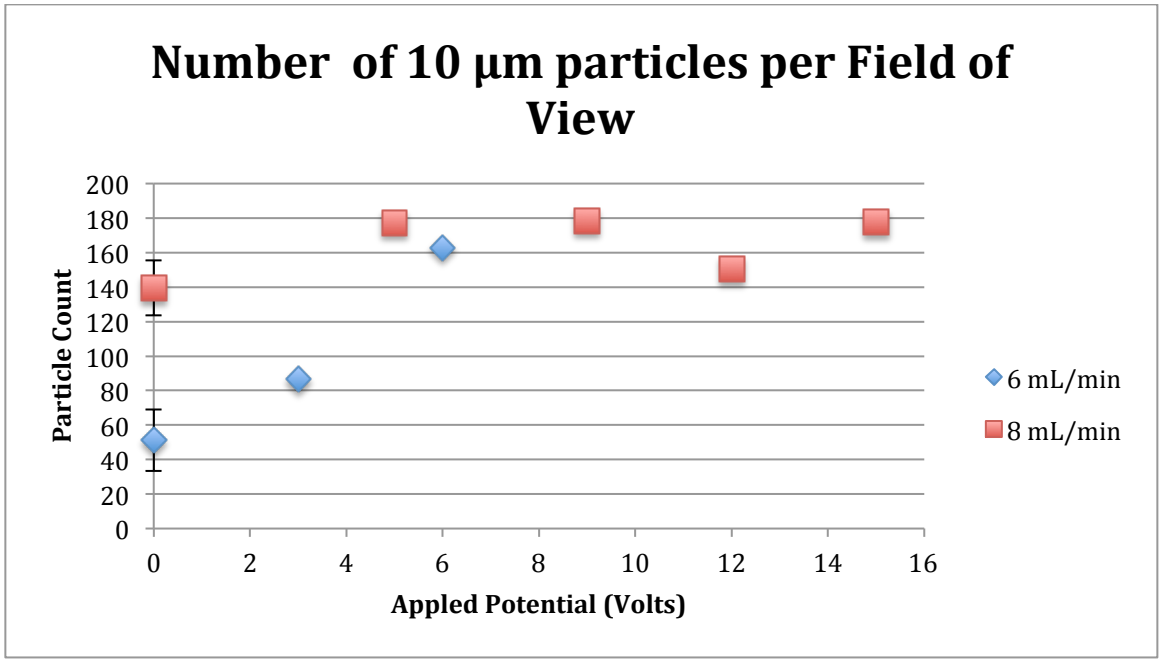

Figure 52 -- Plot of counts of 10 μm particles for the two experimental flow rates.

References:

1. Molla, S.H. and S. Bhattacharjee, *Prevention of colloidal membrane fouling employing dielectrophoretic forces on a parallel electrode array.* Journal of Membrane Science, 2005. **255**(1-2): p. 187-199.
2. Kuberkar, V., P. Czekaj, and R. Davis, *Flux enhancement for membrane filtration of bacterial suspensions using high-frequency backpulsing.* Biotechnology and Bioengineering, 1998. **60**(1): p. 77-87.
3. Kyllˆnen, H.M., P. Pirkonen, and M. Nystrˆm, *Membrane filtration enhanced by ultrasound: a review.* Desalination, 2005. **181**(1-3): p. 319-335.
4. Sundaram, S., et al., *Application of Membrane Filtration for Removal of Diminutive Bioburden Organisms in Pharmaceutical Products and Processes.* PDA Journal of Pharmaceutical Science and Technology, 1999. **53**(4): p. 186-201.
5. Nywening, J.-P. and H. Zhou, *Influence of filtration conditions on membrane fouling and scouring aeration effectiveness in submerged membrane bioreactors to treat municipal wastewater.* Water Research, 2009. **43**(14): p. 3548-3558.
6. *National Health Care Expenditure Data*, 2010, Centers for Medicare and Medicaid Services, Office of the Actuary, National Health Statistics Group.
7. Mannoor, M.S., et al., *Electrical detection of pathogenic bacteria via immobilized antimicrobial peptides.* Proceedings of the National Academy of Sciences, 2010. **107**(45): p. 19207-19212.
8. Esserman, L.J., et al., *A role for biomarkers in the screening and diagnosis of breast cancer in younger women.(Report).* Expert Review of Molecular Diagnostics, 2007. **7**(5): p. 533(12).
9. Kusiak, A., B. Dixon, and S. Shah, *Predicting survival time for kidney dialysis patients: a data mining approach.* Computers in Biology and Medicine, 2005. **35**(4): p. 311-327.
10. Du, F., et al., *Dielectrophoretically intensified cross-flow membrane filtration.* Journal of Membrane Science, 2009. **336**(1-2): p. 71-78.
11. Smith, P.J., et al., *Productivity enhancement in a cross-flow ultrafiltration membrane system through automated de-clogging operations.* Journal of Membrane Science, 2006. **280**(1-2): p. 82-88.
12. Toner, M. and D. Irimia, *BLOOD-ON-A-CHIP.* Annual Review of Biomedical Engineering, 2005. **7**(1): p. 77-103.
13. Turgeon, M.L., *Clinical Hematology: Theory and Proceduces*. 4th ed 2004: Lippincott Williams & Wilkins. 570.
14. Herr, A.E., et al., *Microfluidic immunoassays as rapid saliva-based clinical diagnostics.* Proceedings of the National Academy of Sciences, 2007. **104**(13): p. 5268-5273.
15. Pohl, H.A., *Dielectrophoresis* 1978, Cambridge: Cambridge University Press.
16. JONES, T.B., *Basic Theory of Dielectrophoresis and Electrorotation*, in *IEEE ENGINEERING IN MEDICINE AND BIOLOGY MAGAZINE*2003. p. 33-42.

17. Khoshmanesh, K., et al., *Dielectrophoretic Platforms for Bio-microfluidic Systems.* Biosensors and Bioelectronics. **26**(5): p. 15.
18. Pethig, R., et al., *Dielectrophoresis: A Review of Applications for Stem Cell Research.* Journal of Biomedicine and Biotechnology, 2010: p. 7.
19. Wang, X.-B., et al., *Separation of Polystyrene Microbeads Using Dielectrophoretic/Gravitational Field-Flow-Fractionation.* Biophysical journal, 1998. **74**(5): p. 2689-2701.
20. Choi, S. and J.-K. Park, *Microfluidic system for dielectrophoretic separation based on a trapezoidal electrode array.* Lab on a Chip, 2005. **5**(10): p. 1161-1167.
21. CUMMINGS, E.B., *Streaming Dielectrophoresis for Continuous-Flow Microfluidic Devices*, in *IEEE ENGINEERING IN MEDICINE AND BIOLOGY MAGAZINE*2003. p. 75-84.
22. Hwang, K.-J., C.-Y. Liao, and K.-L. Tung, *Effect of membrane pore size on the particle fouling in membrane filtration.* Desalination, 2008. **234**(1-3): p. 16-23.
23. Hong, S., R.S. Faibish, and M. Elimelech, *Kinetics of Permeate Flux Decline in Crossflow Membrane Filtration of Colloidal Suspensions.* Journal of Colloid and Interface Science, 1997. **196**(2): p. 267-277.
24. Pontie, M., et al., *Preparation and characterization of an electronically conductive and chemically modified ultrafiltration type membrane.* Journal of Membrane Science, 2001. **184**: p. 165-173.
25. Kang, K.H., et al., *Effects of dc-dielectrophoretic force on particle trajectories in microchannels.* Journal of Applied Physics, 2006. **99**(6): p. 064702-8.
26. Kang, Y., et al., *Continuous particle separation with localized AC-dielectrophoresis using embedded electrodes and an insulating hurdle.* Electrochimica Acta, 2009. **54**(6): p. 1715-1720.
27. Millipore™: Billerica, MA.
28. Hiemenz, P.C., *Principles of Colloid and Surface Chemistry*. 3rd ed1997: CRC Press.
29. Kim, I.C. and S. Torquato, *Effective conductivity of suspensions of hard spheres by Brownian motion simulation.* J. Appl. Phys., 1991. **69**(4): p. 2280-2289.